Mon. Not. R. Astron. Soc. (2005) doi:10.1111/j.1365-2966.2005.09419.x

Redshift estimation of clusters by wavelet decomposition of their Sunyaev–Zel'dovich morphology

B. M. Schäfer,[1⋆] C. Pfrommer[1⋆] and S. Zaroubi[1,2⋆]

[1]*Max-Planck-Institut für Astrophysik, Karl-Schwarzschild-Strasse 1, Postfach 1317, 85741 Garching, Germany*
[2]*Kapteyn Astronomical Institute, University of Groningen, Landleven 12, 9747 AG Groningen, the Netherlands*

Accepted 2005 July 11. Received 2005 July 7; in original form 2003 October 23

ABSTRACT

A method for estimating redshifts of galaxy clusters based solely on resolved Sunyaev–Zel'dovich (SZ) images is proposed. Given a high-resolution SZ cluster image (with a FWHM of ∼1 arcmin), the method indirectly measures its structure-related parameters (amplitude, size, etc.) by fitting a model function to the higher-order wavelet moments of the cluster's SZ morphology. The applicability and accuracy of the wavelet method are assessed by applying the method to maps of a set of clusters extracted from hydrodynamical simulations of cosmic structure formation. The parameters, derived by a fit to the spectrum of wavelet moments as a function of scale, are found to show a dependence on redshift z that is of the type $x(z) = x_1 \exp(-z/x_2) + x_3$, where the monotony of this functional behaviour and the non-degeneracy of those parameters allow inversion and estimation of the redshift z. The average attainable accuracy in the z estimation relative to $1 + z$ is ∼4–5 per cent out to $z \simeq 1.2$, which is comparable with photometric redshifts. For single-frequency SZ interferometers, in which the ambient fluctuating CMB is the main noise source, the accuracy of the method drops slightly to $\langle \Delta z/(1+z) \rangle \sim 6$–7 per cent. Other complications addressed include instrumental noise, cold cores and systematic trends in baryon fraction with cluster mass.

Key words: methods: numerical – galaxies: clusters: general – cosmic microwave background – distance scale.

1 INTRODUCTION

Inverse Compton scattering of cosmic microwave background (CMB) photons off thermal electrons of the hot intracluster medium (ICM) of galaxy clusters produces fluctuations in the surface brightness of the CMB, an effect known as the thermal Sunyaev–Zel'dovich (SZ) effect (e.g. Sunyaev & Zel'dovich 1972, 1980; Rephaeli 1995). Imaging clusters of galaxies through their SZ signature has, until recently, been a very challenging undertaking. To date, the development of detectors and new techniques have allowed high-quality interferometric imaging of more than 50 clusters of galaxies (Carlstrom, Holder & Reese 2002), despite incomplete coverage of the Fourier plane. In the foreseeable future, the availability of detectors in the microwave regime with angular resolutions surpassing 1 arcmin and sensitivities in the μK range (e.g. the South Pole Telescope, described in detail in Carlstrom et al. 2002) will enable the hot plasma in galaxy clusters to be probed out to large redshifts, providing SZ-based wide-field galaxy cluster catalogues and yielding a multitude of information about cluster formation and the cosmological model (Birkinshaw 1999).

⋆E-mail: spirou@mpa-garching.mpg.de (BMS); pfrommer@mpa-garching.mpg.de (CP); S.Zaroubi@astro.rug.nl (SZ)

In particular, the abundance of clusters as a function of redshift has been shown to be a very sensitive probe of the cosmological model (Eke et al. 1998; Henry 2000). The near independence of the line-of-sight SZ amplitude and cluster redshift makes the SZ effect the main tool for detecting galaxy clusters at high redshifts ($0.5 \lesssim z \lesssim 2$, where the upper limit depends sensitively on cosmology). This range of redshifts is especially important for probing the nature of the dark energy of the Universe, since during this era it is expected to evolve rapidly until it eventually dominates over the other cosmological fluids. In order to obtain precise constraints on cosmological models it is essential to have accurate measurements of the redshift distribution of galaxy clusters (see Haiman, Mohr & Holder 2001).

Normally, one determines the distance to the cluster by photometric or spectroscopic observations of the cluster member galaxies. Unfortunately, this is a very challenging and time-consuming task, in particular when one considers the very large number of high-redshift clusters expected to be observed with future sensitive SZ instruments – the *Planck* satellite alone is expected to detect about 10^4 clusters (Bartelmann 2001). In order to replace photometric follow-ups we aim at inferring the distance to a cluster from SZ data alone for a future generation of experiments with increased angular resolution of about 1 arcmin.

Theoretically, the cold dark matter (CDM) hierarchical clustering paradigm predicts a universal profile for dark matter haloes

that depends on only two parameters: core radius and concentration (Navarro, Frenk & White 1995). In addition, the same theory provides a very simple recipe for the mass-accretion history of a given halo as a function of its formation and observation redshift (Wechsler et al. 2002; van den Bosch 2002; Zhao et al. 2003). Using these relations together with simple assumptions such as hydrostatic equilibrium and isothermality, one can expect that, in the framework of the spherical collapse model, the observable SZ flux and apparent size should provide measures of the cluster's mass and distance.

Indeed, by using scaling relations, Diego et al. (2003) demonstrated the viability of determining reliable *morphological redshifts*, and examined various SZ observables with respect to their distance sensitivity. Among those observables, they showed that the cluster apparent size and central amplitude are promising distance indicators, once their degeneracy is broken.

The main goal of this work is to derive redshifts of clusters based solely on their resolved SZ images by modelling the evolution of their structural parameters with redshift from the data set itself. This phenomenological approach does not depend on a priori assumptions about scaling relations that are valid only for spherically symmetric and relaxed systems.

Specifically, the structural morphology of the cluster's pressure profile in an SZ observation is characterized by wavelet analysis.[1] We are able to show that there is a simple relationship between the distribution of moments over various scales in wavelet space and the cluster properties that can be described with simple phenomenological functions. Furthermore, the parameters of these functions are shown to follow a well-defined and simple redshift dependence. Wavelet analysis has been chosen because it maintains the scale and positional information of cluster morphology, and hence it makes isolation and suppression of various unwanted contributions to the observed signal possible while it reliably upholds the underlying behaviour. We note, however, that Fourier space analysis could in principle yield very similar results.

Hydrodynamically simulated clusters are used to demonstrate the method and to set limits on the redshift uncertainty expected in this approach. The simulated clusters used in the analysis are close to virialization; merging systems, for example, are excluded. Under this restriction, the relationship between the observed quantity and the cluster physical parameters as well as between the observed quantity and the structural parameters are well defined. In addition, simulated clusters ignore radiative and feedback processes, the effect of which is discussed later in the paper.

In the observational application, the evolution of the structural parameters following from wavelet decomposition could be calibrated from a (relatively small) training set of high-quality SZ clusters with known (photometric/spectroscopic) redshifts.

Our method relies crucially on the availability of resolved SZ-cluster images. Therefore, throughout the paper we assume an instrumental resolution of 1 arcmin, for which massive clusters should be resolved even at the largest redshifts considered here. Indeed, future instruments such as the South Pole Telescope[2] (Carlstrom et al. 2002) or the Atacama Cosmology Telescope[3] are designed to yield observations of up to 10^4 galaxy clusters with masses $\gtrsim 10^{14}\,\mathrm{M}_\odot$ (2–10 μK beam^{-1} sensitivity) and $\sim$1-arcmin resolution.

This article is organized as follows. After basic definitions concerning the SZ effect in Section 2, wavelets and wavelet transforms of idealized cluster profiles are introduced in Section 3, and the simulations are outlined in Section 4. The capability of wavelets with respect to distance estimation is examined in Section 5. Possible systematics are addressed in Section 6. A summary of the techniques in Section 7 and of the results in Section 8 concludes the article.

2 SUNYAEV–ZEL'DOVICH DEFINITIONS

The SZ effect has been described in detail by many authors (for a comprehensive review see Birkinshaw 1999); here we briefly review its main aspects. The SZ effect arises because CMB photons experience Compton scattering off electrons of the diffuse intracluster plasma. The CMB spectrum is modulated as photons are redistributed from the low-frequency part of the spectrum below 218 GHz to higher frequencies. The change in thermodynamic CMB temperature arising from the thermal SZ effect is

$$\frac{\Delta T}{T}(\boldsymbol{\phi}) = y(\boldsymbol{\phi})\left(x\frac{\mathrm{e}^x+1}{\mathrm{e}^x-1}-4\right) \simeq -2y(\boldsymbol{\phi}) \quad \text{for } x \ll 1, \tag{1}$$

where $x = h\nu/k_\mathrm{B}T_\mathrm{CMB}$ is the dimensionless frequency. In the Rayleigh–Jeans limit ($x \ll 1$), the change in temperature is asymptotically equal to $-2y(\boldsymbol{\phi})$. The SZ amplitude at location $\boldsymbol{\phi}$, which is known as the Comptonization parameter $y(\boldsymbol{\phi})$, is defined as the line-of-sight integral of the temperature-weighted thermal electron density:

$$y(\boldsymbol{\phi}) = \frac{\sigma_\mathrm{T}k_\mathrm{B}}{m_\mathrm{e}c^2}\int \mathrm{d}l\, n_\mathrm{e}(\boldsymbol{\phi}, l)T_\mathrm{e}(\boldsymbol{\phi}, l), \tag{2}$$

where m_e, c and k_B denote the electron mass, speed of light and Boltzmann's constant, respectively. $T_\mathrm{e}(\boldsymbol{\phi}, l)$ and $n_\mathrm{e}(\boldsymbol{\phi}, l)$ are the electron temperature and electron number density at position $\boldsymbol{\phi}$ and distance l.

3 WAVELETS

3.1 Wavelet definitions

During the last decade, wavelet analysis has become a popular tool in various data analysis and image processing applications. The main appeal of wavelet functional bases stems from their simultaneous localization of a signal in both the wavenumber and position domain, making orthogonal and complete projections on modes belonging to both spaces possible. In particular, the discrete wavelet families, by virtue of their constituting a complete basis, provide a unique and fast decomposition of the images into wavelet expansion coefficients. Statistical analysis in terms of the qth moments of the distribution of wavelet coefficients as a function of scale can compress the signal contained in an image into a small number of parameters and yields information surpassing that derived in traditional Fourier analysis.

Following Daubechies & Bates (1993) and Muzy, Bacry & Arneodo (1993), the wavelet transform of a two-dimensional image is defined as a convolution of the function $y(\boldsymbol{x})$ to be analysed with the wavelet $\psi_\sigma(|\boldsymbol{x}-\boldsymbol{\mu}|)$:

$$\chi(\boldsymbol{\mu}, \sigma) = \int \mathrm{d}^2x\; y(\boldsymbol{x})\cdot\; \psi_\sigma\left(|\boldsymbol{x}-\boldsymbol{\mu}|\right). \tag{3}$$

High values for $\chi(\boldsymbol{\mu}, \sigma)$ are obtained in the case of a match between the features of $y(\boldsymbol{x})$ and the wavelet $\psi_\sigma(\boldsymbol{x})$ at position $\boldsymbol{\mu}$ and

[1] There are, of course, other ways of characterizing the cluster's density profile in an SZ observation that are more or less susceptible to noise, for example the fitting of a β-profile (Cavaliere & Fusco-Femiano 1978) to the electron density.

[2] http://astro.uchicago.edu/spt/

[3] http://www.hep.upenn.edu/~angelica/act/act.html

scale σ. From the wavelet expansion coefficients $\chi(\boldsymbol{\mu}, \sigma)$ on scale σ at location $\boldsymbol{\mu}$ one obtains the wavelet moments $X_q(\sigma)$ by integration over all displacements $\boldsymbol{\mu}$:

$$X_q(\sigma) = \int \mathrm{d}^2\mu \; |\chi(\boldsymbol{\mu}, \sigma)|^q \,. \tag{4}$$

The exponent $q \in \mathbb{N}$ defines the order of the wavelet moment $X_q(\sigma)$. Values for q equal to or larger than 2 allow noise suppression. The logarithm $\ln X(\sigma, q)$ of the wavelet moment as a function of logarithmic scale $\ln \sigma$ constitutes the wavelet spectrum. The $X_q(\sigma)$-statistic is the main tool used in this study for characterizing the morphology of SZ clusters.

3.2 Application of wavelets to a cluster profile

3.2.1 Analytic wavelet transform of a cluster ***y****-profile*

In order to illustrate our idea of determining cluster sizes via wavelet decomposition, the wavelet transform of a King profile, which is known to describe the SZ morphology of clusters to first order, is performed. As an analysing wavelet, the Mexican-hat wavelet was chosen for simplicity.

It is advantageous to compute the convolution in the definition of $\chi(\boldsymbol{\mu}, \sigma)$ in the Fourier domain. By virtue of equation (6), namely

$$\chi(\boldsymbol{\mu}, \sigma) = \int \mathrm{d}^2x \; y(\boldsymbol{x}) \; \psi_\sigma(\boldsymbol{x} - \boldsymbol{\mu}) \tag{5}$$

$$= (2\pi)^2 \int \mathrm{d}^2k \; Y(\boldsymbol{k}) \; \Psi_\sigma(-\boldsymbol{k}) \exp(\mathrm{i}\boldsymbol{k}\boldsymbol{\mu}), \tag{6}$$

the convolution reduces to a mere multiplication of the Fourier transforms $Y(\boldsymbol{k})$ and $\Psi_\sigma(\boldsymbol{k})$ of the image $y(\boldsymbol{x})$ and the wavelet $\psi_\sigma(\boldsymbol{x})$, respectively. Restricting the order of the wavelet moment to $q = 2$ and inserting the convolution theorem (6) into the definition (4) yields

$$X_2(\sigma) = (2\pi)^4 \int \mathrm{d}^2\mu \; \left| \int \mathrm{d}^2k \; Y(\boldsymbol{k}) \Psi_\sigma(-\boldsymbol{k}) \exp(\mathrm{i}\boldsymbol{k}\boldsymbol{\mu}) \right|^2 \tag{7}$$

$$= (2\pi)^6 \int \mathrm{d}^2k \, |Y(\boldsymbol{k})|^2 \, |\Psi_\sigma(\boldsymbol{k})|^2 \,, \tag{8}$$

where the replacement $|\Psi_\sigma(-\boldsymbol{k})|^2 = |\Psi_\sigma(\boldsymbol{k})|^2$ holds for real wavelets.

The Mexican-hat wavelet is defined as the negative second derivative of a Gaussian:

$$\psi_{\mathrm{MH}}(\boldsymbol{x}) = \psi_{\mathrm{MH}}(x) = -\nabla_{\boldsymbol{x}}^2 \left[\frac{1}{2\pi\sigma^2} \exp\left(-\frac{\boldsymbol{x}^2}{2\sigma^2} \right) \right], \tag{9}$$

whereof the Fourier transform $\Psi_{\mathrm{MH}}(\boldsymbol{k})$ is derived by twofold partial integration:

$$\Psi_{\mathrm{MH}}(k) = \int \frac{\mathrm{d}^2x}{(2\pi)^2} \; \psi_{\mathrm{MH}}(\boldsymbol{x}) \exp(-\mathrm{i}\boldsymbol{k}\boldsymbol{x}) \tag{10}$$

$$= \frac{1}{(2\pi)^2\sigma^6} \int r\mathrm{d}r(2\sigma^2 - r^2) \exp\left(-\frac{r^2}{2\sigma^2} \right) J_0(kr) \tag{11}$$

$$= \frac{k^2}{(2\pi)^2} \exp\left(-\frac{k^2\sigma^2}{2} \right), \tag{12}$$

where the azimuthal symmetry and the definition of the zeroth-order Bessel function of the first kind, $2\pi J_0(kr) = \int_0^{2\pi} \mathrm{d}\phi \exp(\mathrm{i}kr\cos\phi)$ was used in the first step. Thus, the Fourier transform of the wavelet, $\Psi_\sigma(k)$, is given by the Hankel transform of the second derivative of a Gaussian.

For the determination of $Y(\boldsymbol{k})$, we assume that the projected thermal electron density can be described by a spherically symmetric King profile, i.e. a β-model (Cavaliere & Fusco-Femiano 1978) with $\beta = 1$, core radius r_c and central value of the Comptonization parameter y_0:

$$y(\boldsymbol{x}) = y(r) = y_0 \left[1 + \left(\frac{r}{r_\mathrm{c}} \right)^2 \right]^{-1}. \tag{13}$$

Then, the Fourier transform is easily computed:

$$Y(k) = \int \frac{\mathrm{d}^2x}{(2\pi)^2} \; y(\boldsymbol{x}) \exp(-\mathrm{i}\boldsymbol{k}\boldsymbol{x}) \tag{14}$$

$$= \frac{y_0 r_\mathrm{c}^2}{2\pi} \int \mathrm{d}r \; \frac{r}{r_\mathrm{c}^2 + r^2} J_0(kr) = \frac{y_0 r_\mathrm{c}^2}{2\pi} \; K_0(kr_\mathrm{c}), \tag{15}$$

where in equation (15) the definition of the zeroth-order modified Bessel function of the second kind, $K_0(kr_\mathrm{c})$, was inserted.

Substitution of equations (12) and (15) into equation (8) and exploitation of the azimuthal symmetry of the functions $y(\boldsymbol{x})$ and $\psi(\boldsymbol{x})$ yields an analytic integral for $X_2(\sigma)$:

$$X_2(\sigma) = 2\pi y_0^2 r_\mathrm{c}^4 \int_0^\infty \mathrm{d}k \; k^5 \exp(-\sigma^2k^2) K_0^2(kr_\mathrm{c}). \tag{16}$$

After evaluation of the integral in equation (16), the wavelet transform of the β-profile reads as follows:

$$X_2(\sigma) = \frac{\pi^{3/2} y_0^2}{2r_\mathrm{c}^2} \; \alpha^6 \mathcal{G}_{2,3}^{3,1}\left(\alpha^2 \Big|_{0\,0\,0}^{-2\;\frac{1}{2}} \right), \tag{17}$$

where the substitution $\alpha = r_\mathrm{c}/\sigma$ has been made. The function $\mathcal{G}$ is Meijer's G-function, the exact definition of which is given by Gradshteyn & Ryzhik (1994). It is an interesting consistency to note that, apart from the normalization, the functional shape of equation (17) depends only on α; that is, on the core radius r_c expressed in units of the wavelet scale σ.

3.2.2 Asymptotics of the analytical wavelet transform

The asymptotic behaviour of $X_2(\sigma)$ at the limit of $\sigma \ll r_\mathrm{c}$ can be explored by substituting the expressions given in equations (13) and (9) into equation (6), and exchanging, by partial integration, the function on which the Laplacian operates. In the limit of interest the Gaussian can be replaced by a Dirac-δ distribution. Substituting all of this into equation (4) yields that $\lim_{\sigma\to 0} X_2(\sigma)$ is proportional to y_0^2 and independent of σ; that is, the normalization of the wavelet spectrum measures the square of the central Comptonization parameter y_0:

$$X_2(\sigma) = \frac{32\pi}{15} \; \frac{y_0^2}{r_\mathrm{c}^2} \qquad \text{for} \qquad \sigma \ll r_\mathrm{c}. \tag{18}$$

In the opposite limit, i.e. $r_\mathrm{c} \ll \sigma$, one can use the fact that the King profile is highly peaked at the centre and that it is convolved with a Mexican-hat wavelet, guaranteeing the convergence of the integral in equation (16) at ∞. In the limit of $r_\mathrm{c} \to 0$ this integral is dominated by the value at $k = 0$. Therefore, one can approximate the King profile with a Dirac-δ distribution and show that asymptotically $\lim_{r_\mathrm{c}\to 0} X_2(\sigma)$ is proportional to σ^{-6}:

$$X_2(\sigma) \propto \frac{y_0^2 r_\mathrm{c}^4}{\sigma^6} \qquad \text{for} \qquad \sigma \gg r_\mathrm{c}. \tag{19}$$

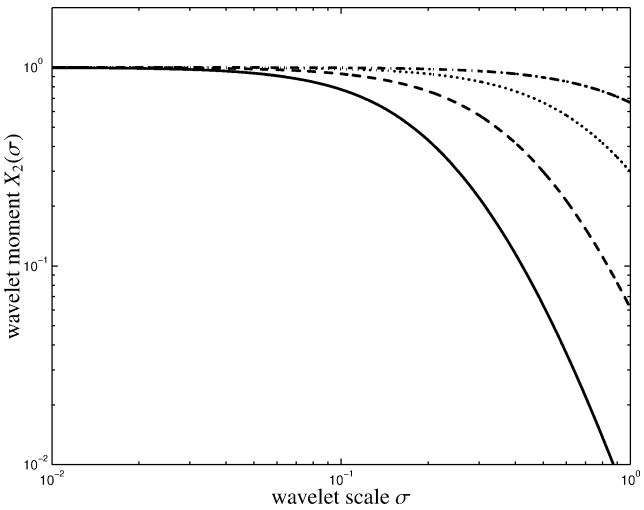

Figure 1. Sensitivity of the wavelet spectrum to the cluster size. The second-order wavelet moments $X_2(\sigma)$ are shown as a function of σ for various core sizes $r_c = 0.5$ (solid), $r_c = 1$ (dashed), $r_c = 2$ (dotted) and $r_c = 4$ (dot–dashed). The curves have been normalized to their asymptotic values for $\sigma \to 0$.

The sensitivity of the wavelet spectrum $X_2(\sigma)$ to cluster size r_c is illustrated in Fig. 1. The wavelet spectrum is constant for $\sigma \ll r_c$, has an r_c-dependent break and drops off asymptotically $\propto \sigma^{-6}$ for $\sigma \gg r_c$. Naturally, the scale σ, at which the transition from one asymptotic regime to the other occurs, is determined by the value of r_c, i.e. by the cluster size.

With this example in mind, the wavelet moments $X_q(\sigma)$ obtained from real data (Section 5.3) will be fitted with a power law with an exponential cut-off, where the cut-off indicates the cluster size and the amplitude is proportional to some power of the central Comptonization parameter y_0.

3.2.3 Finite instrumental resolution

The influence of finite instrumental resolution can easily be incorporated by an additional factor $|B(k)|^2$ in equation (8):

$$X_2(\sigma) = (2\pi)^6 \int \mathrm{d}^2k\, |Y(k)|^2\, |\Psi_\sigma(k)|^2\, |B(k)|^2\,, \tag{20}$$

where $B(k)$ is the Fourier transform of the (azimuthally symmetric) beam profile $b(x)$, which is for simplicity assumed to be of Gaussian shape with FWHM $= \sqrt{8\ln(2)}\,\sigma_b$:

$$B(k) = \int \frac{\mathrm{d}^2x}{(2\pi)^2}\, b(x) \exp(-\mathrm{i}\boldsymbol{k}\boldsymbol{x}) \text{ with} \tag{21}$$

$$b(\boldsymbol{x}) = \frac{1}{2\pi\sigma_b^2} \exp\left(-\frac{\boldsymbol{x}^2}{2\sigma_b^2}\right). \tag{22}$$

This effectively replaces σ in equation (17) by the harmonic mean $\sqrt{\sigma^2 + \sigma_b^2}$, which limits the range of accessible wavelet scales to $\sigma > \sigma_b$.

3.3 Analogy to power spectra in Fourier analysis

By interpreting the wavelet spectrum in equation (8) as the variance of the fluctuations on the scale σ, it is possible to draw an analogy to Fourier decomposition:

$$\mathrm{var}\,[y(x)] = X_2(\sigma) = (2\pi)^4 \int \mathrm{d}^2k\; P(k)\, |\Psi_\sigma(k)|^2\,, \tag{23}$$

where $P(k) = (2\pi)^2 \langle |Y(k)|^2 \rangle$ is the Fourier power spectrum. The wavelet $\psi(x)$ now adopts the role of a filter function on scale σ. This filter function reads in real space, in the case of the Mexican-hat wavelet, as

$$\psi_{\mathrm{MH}}(\boldsymbol{x}) = \frac{2\sigma^2 - \boldsymbol{x}^2}{2\pi\sigma^6} \exp\left(-\frac{\boldsymbol{x}^2}{2\sigma^2}\right). \tag{24}$$

Therefore, our method is equivalent to considering power spectral analysis of filtered fields and higher-order Fourier space moments.

4 SIMULATIONS

The accuracy in the determination of redshift z was assessed by examining the performance on numerical simulations. First, simulations of cosmological structure formation including gas physics were carried out in order to model the evolution of clusters (Section 4.1). Subsequently, maps of the Compton-y parameter were produced by using an interpolation kernel with an adaptive smoothing length for projecting the Compton-y parameter along the line of sight (Section 4.2). By applying selection criteria favouring virialized systems a cluster sample was compiled (Section 4.3). Finally, with the aim of realistic single-frequency SZ observations, we simulated the ambient CMB fluctuations that act as the primary source of noise (Section 4.4) and combined the resulting realizations of the CMB with the cluster maps (Section 4.5).

The assumed cosmological model is the standard ΛCDM cosmology, which has recently been supported by findings from the *WMAP* satellite (Bennett et al. 2003; Spergel et al. 2003). Parameter values have been chosen as $\Omega_M = 0.3$, $\Omega_\Lambda = 0.7$, $H_0 = 100\,h$ km s^{-1} Mpc^{-1} with $h = 0.7$, $\Omega_B = 0.04$, $n_s = 1$ and $\sigma_8 = 0.9$.

4.1 Smoothed particle hydrodynamic cluster simulations

A simulation of cosmological structure formation kindly provided by V. Springel and L. Hernquist (Springel & Hernquist 2002; White, Hernquist & Springel 2002) constitutes the basis of our analysis. In a cubic box of comoving side length 100 Mpc h^{-1} with periodic boundary conditions, a smoothed particle hydrodynamic (SPH) simulation comprising 216^3 dark matter particles as well as 216^3 gas particles was run and snapshots were saved at 23 redshifts ranging from $z = 0.102$ out to $z = 1.114$. The comoving spacing along the line of sight of two subsequent boxes was 100 Mpc h^{-1}. Adiabatic gas physics and shock heating were included, but radiative cooling and star formation were ignored, which does not result in significant differences in SZ morphology, as shown by White et al. (2002), but does impact on the scaling relations, as demonstrated by da Silva et al. (2001).

Overdensities are identified using a friends-of-friends algorithm with the linking length $b = 0.164$, which yields all member particles of a cluster in conjunction with a spherical overdensity code, from which virial quantities are estimated. We computed the mass M_{vir} inside a sphere of radius r_{vir}, interior to which the average density was 200 times the critical density $\rho_{\mathrm{crit}} = 3H_0^2/(8\pi G)$. The angle subtended by twice the virial radius is denoted as θ_{vir}. We imposed a lower mass threshold of $M_{\mathrm{vir}} \geqslant 5 \times 10^{13}\,\mathrm{M}_\odot\,h^{-1}$.

The simulation used here seems to be appropriate for assessing the redshift estimation accuracy for a number of reasons. It provides a large number of suitable systems, so that the influence of morphological variety can be studied, and the clusters are very well resolved with respect to their baryonic profiles. Furthermore, the cluster's evolution has been modelled taking into account their cosmological environment.

A justified objection might be that the simulation is biased toward low-mass systems, because high-mass systems form less frequently, and, especially in small simulation boxes, the high-mass end of the Press–Schechter function is sampled insufficiently. This shortcoming could be remedied by using simulations of single objects, but in the simulation at hand it would have been difficult to accumulate sufficient statistics, or by using even larger simulation boxes while upholding the mass resolution, which rapidly becomes computationally unfeasible.

4.2 SZ map preparation

Square maps of the Compton-y parameter of the selected clusters were generated by SPH projection of all member gas particles onto a cubic grid with 128^2 mesh points. The (comoving) side length s of the map was adapted to the cluster size, such that the comoving resolution $g = s/128$ of the grid is specific to a given map. Examples of SZ maps are given in Fig. 2.

If the particle p at position $\boldsymbol{r}_p = (x_p, y_p, z_p)$ has a smoothing length h_p, an SPH electron number density estimate n_p, and an SPH electron temperature T_p, the Compton-y parameter at the pixel at position $\boldsymbol{x}$ is given by

$$y(\boldsymbol{x}) = \frac{\sigma_\mathrm{T} k_\mathrm{B}}{m_\mathrm{e} c^2} \frac{h_p^3}{g^2} \sum_p \left[\int_{x-g/2}^{x+g/2} \mathrm{d}x_p \int_{y-g/2}^{y+g/2} \mathrm{d}y_p \int_{-h_p}^{h_p} \mathrm{d}z_p \, \mathcal{K}\left(\frac{r}{h_p}\right) n_p T_p \right] \tag{25}$$

$$\text{with } r = \sqrt{(x_p - x)^2 + (y_p - y)^2 + z_p^2}. \tag{26}$$

Here, we assumed complete ionization and primordial element composition of the ICM for the determination of electron number density and temperature. In this way we produced projections along each of the three coordinate axes. The function $\mathcal{K}$ is the spherically symmetric cubic spline kernel suggested by Monaghan & Lattanzio (1985), which was also used in the SPH simulation:

$$\mathcal{K}(u) = \frac{8}{\pi} \begin{cases} 1 - 6u^2 + 6u^3, & 0 \leqslant u \leqslant 1/2 \\ 2(1-u)^3 & , \quad 1/2 < u \leqslant 1 \text{ with } u = r/h_p. \\ 0 & , \quad u > 1 \end{cases} \tag{27}$$

The fact that the kernel $\mathcal{K}$ is defined on a compact support $u \in [0 \ldots 1]$ greatly reduces the computational effort required.

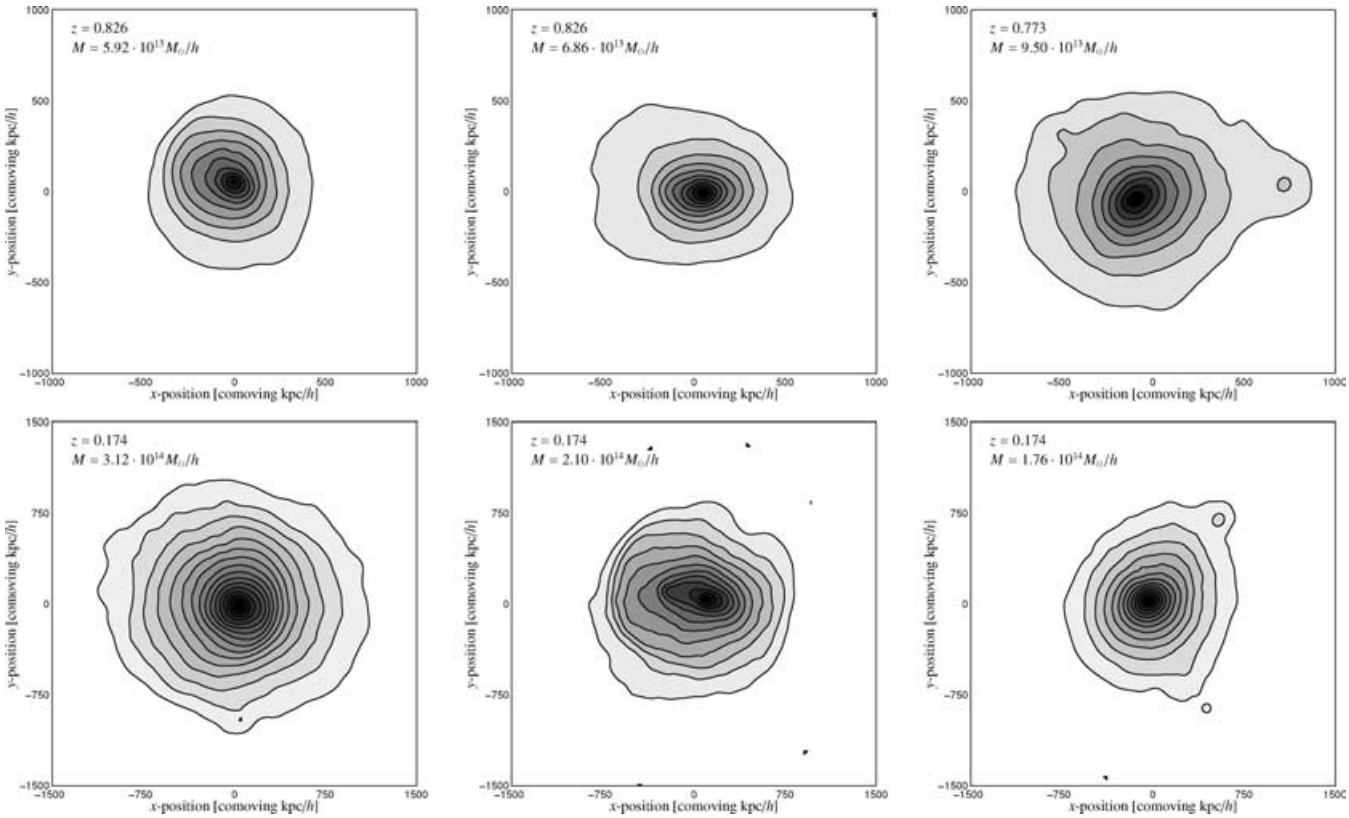

Figure 2. Picture book of Sunyaev–Zel'dovich clusters. The upper panel shows clusters at high redshifts of $z \simeq 0.8$, to be compared with clusters at low redshifts of $z = 0.174$ in the lower panel. The columns contrast different morphologies in an exemplary fashion: relaxed systems (left column), elongated clusters (centre column) and clusters in the phase of minor merging or mass accretion (right column). The grey-scale denotes the amplitude of $y(\boldsymbol{x})' = \log[1 + 10^5\, y(\boldsymbol{x})]$ and the contours have a logarithmically equidistant spacing of 0.1 dex, i.e. the lowest contour denotes a common value of $y = 2.5 \times 10^{-6}$. All of the clusters depicted above meet the selection criteria discussed in Section 4.3.

4.3 Cluster selection

Clearly, the wavelet redshift estimation relies on the fact that clusters are not in a state of violent merging, such that the cluster observables, namely the apparent size and integrated SZ flux, are linked via scaling relations. Secondly, the wavelet analysis derives a single parameter describing the extension of the cluster from the break in the spectrum $X_q(\sigma)$ of wavelet parameters, and hence elongated clusters should be excluded from the analysis, because in those systems the extension cannot be measured unambiguously. Consequently, apart from the minimal mass of $M_{\rm min} = 5 \times 10^{13}\,{\rm M}_\odot\,h^{-1}$, which translates into a minimally required line-of-sight Comptonization amplitude $y_{\rm min}$, clusters have been selected in order to show neither double cores nor pronounced substructure. From the resulting sample, 10 clusters were selected randomly from each redshift bin. In this sample, the ellipticity and the residual deviation from a β-profile were measured, in order to provide a solid quantification.

(i) The SZ morphology is required to be not too elongated. By fitting a two-dimensional β-model $y_\beta(\boldsymbol{x})$ to the SZ profile $y_{\rm data}(\boldsymbol{x})$, values for the semi-axes r_x and r_y are derived. 90 per cent of the clusters within the selected sample have axis ratios $q = r_y/r_x$ greater than 0.8 and ellipticities $e = \sqrt{r_x^2 - r_y^2}/r_x$ below 0.6.

(ii) Residual deviations from the canonical β-profile ought to be small. The rms deviation v of the cluster from the best-fitting β-profile,

$$v = \sqrt{\left\langle \left(\frac{y_{\rm data}(\boldsymbol{x}) - y_\beta(\boldsymbol{x})}{y_\beta(\boldsymbol{x})} \right)^2 \right\rangle_{\boldsymbol{x}}}, \tag{28}$$

was smaller than 25 per cent for 90 per cent of our clusters. In the derivation of v, the region inside the virial radius was considered.

The 10 selected clusters from each of the 23 redshift bins yielded, with the three orthogonal projections of each cluster, a total number of 690 maps with which the accuracy of the wavelet method in estimating redshifts was assessed. The distributions of the ellipticities e and the integrated residuals v are shown in Fig. 3. The same distributions were derived for the smoothed cluster maps, in which the effects of finite instrumental resolution have been incorporated. As Fig. 3 suggests, the beam does not have a major impact on the morphological properties of most of the cluster sample – this is because of the narrowness of the beam (only 1 arcmin FWHM).

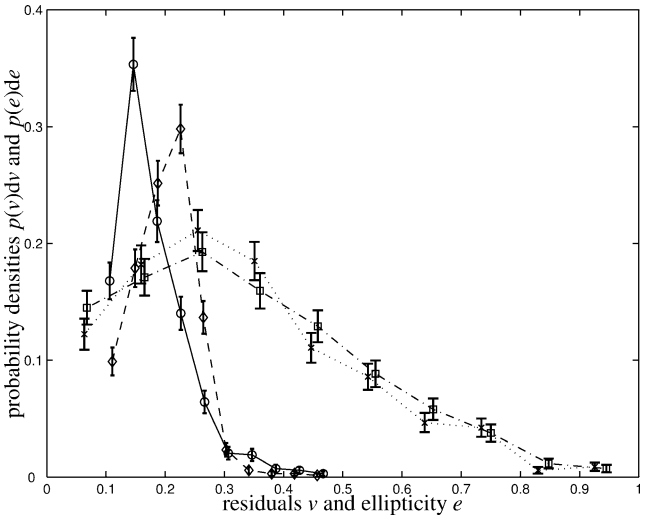

Figure 3. Selection criteria: distribution of residual deviations v from the best-fitting β-profile for unsmoothed (solid, circles) and smoothed (dashed, diamonds) maps. The second set of lines shows the distribution of the ellipticities e with (dot–dashed, squares) and without (dotted, crosses) smoothing.

It should be emphasized that the selection by geometric criteria is more stringent than the requirement of approximate relaxation: while a scatter in the relation of the SZ observables with mass is admissible, only regular systems without double cores or pronounced elongation can be reliably described by the morphological wavelet parameters we consider here.

4.4 CMB map generation

CMB anisotropies are assumed to be a particular realization of a *Gaussian random field*. With the aim of simulating a realization of the CMB on a square, flat map, we take temperature fluctuations $\theta(\boldsymbol{\phi})$ relative to the average CMB temperature of $\langle T \rangle = 2.726\,{\rm K}$ to be the independent random field:

$$\theta(\boldsymbol{\phi}) \equiv \frac{T(\boldsymbol{\phi}) - \langle T \rangle}{\langle T \rangle}. \tag{29}$$

The flat, two-dimensional power spectrum $P_\theta(\ell)$ is defined via

$$\left\langle \Theta(\boldsymbol{\ell})\Theta^*(\boldsymbol{\ell}') \right\rangle \equiv (2\pi)^{-2}\delta_{\rm D}(\boldsymbol{\ell} - \boldsymbol{\ell}')P_\theta(|\boldsymbol{\ell}|), \tag{30}$$

where $\Theta(\boldsymbol{\ell})$ denotes the Fourier transform of $\theta(\boldsymbol{\phi})$. The simulation of the CMB temperature fluctuations on a flat square map now consists of the following two steps.

(i) The angular power spectrum C_ℓ is computed for the flat ΛCDM universe using the CMBFAST code by Seljak & Zaldarriaga (1996). In addition to the cosmological parameters described in Section 4, we use adiabatic initial conditions and set the primordial He mass fraction to $X_{\rm He} = 0.24$ and the Thomson optical depth to $\tau = 0.17$ (Spergel et al. 2003). The angular power spectrum of the CMB is normalized to *COBE* data. Since the SZ effect distorts the CMB only on small angular scales, the flat-sky approximation $\ell \gg 1$ is fulfilled and it is appropriate to replace the spherical harmonics with plane waves. Hu (2000) has shown that the two-dimensional flat power spectrum $P_\theta(\ell)$ is approximately equal to its angular analogue: $C_\ell \simeq P_\theta(\ell)$.

(ii) Then, Gaussian random variables are generated on a complex two-dimensional grid in Fourier space with variance $\sigma^2(\ell) = P_\theta(\ell)$ according to the absolute value of their wavevectors $\boldsymbol{\ell}$. The inverse Fourier transform brings the elementary waves to interference and yields a realization of the temperature anisotropies $\theta(\boldsymbol{\phi})$.

4.5 Simulated single-frequency SZ observations

For SZ clusters observed with a single-frequency interferometer (e.g. the CBI experiment, Halverson et al. 2002),[4] it is important to examine the applicability of the $X_q(\sigma)$-statistic. For the purpose of this paper, it suffices to consider observations at small frequencies ν. Thus, the Compton-y maps are combined with realizations of the CMB fluctuations by using equation (1) in the Rayleigh–Jeans limit:

$$T(\boldsymbol{\phi}) = [1 - 2y(\boldsymbol{\phi})]\,[1 + \theta(\boldsymbol{\phi})]\,\langle T \rangle. \tag{31}$$

Fig. 4 shows the Compton-y map of a nearby cluster of $2.2 \times 10^{14}\,{\rm M}_\odot\,h^{-1}$ at redshift $z = 0.102$ combined with a patch of the CMB constructed by the algorithm described above. In this

[4] http://www.astro.caltech.edu/∼tjp/CBI/

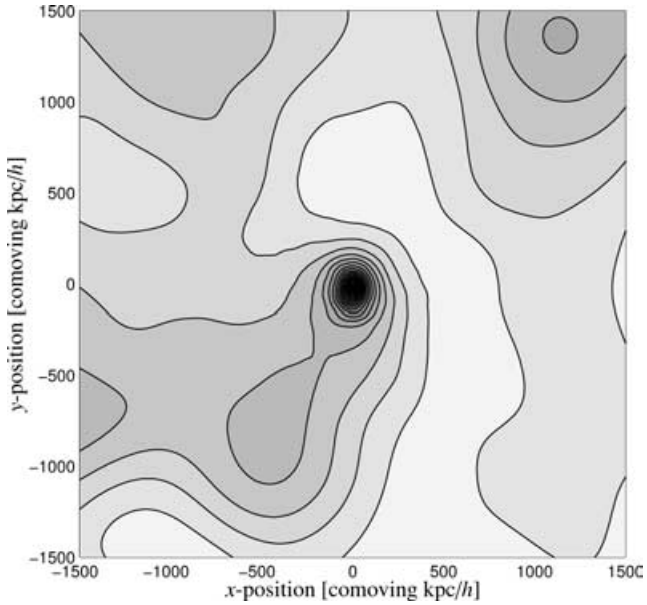

Figure 4. Simulated temperature map of the CMB combined with a foreground SZ cluster at $z = 0.102$ with virial quantities $M_{\rm vir} = 2.2 \times 10^{14}\,{\rm M}_{\odot}/h$, $r_{\rm vir} = 1.47\,{\rm Mpc}\,h^{-1}$ and $k_{\rm B}T_{\rm vir} = 1.52\,{\rm keV}$. At the cluster centre, the SZ temperature decrement amounts to -1.8 mK and the CMB temperature fluctuation with the highest amplitude is equal to 0.23 mK. A total of 30 linearly spaced isothermals are drawn. In this case, the comoving scale 1 Mpc/h corresponds to 11.5 arcmin.

map, the average CMB temperature $\langle T \rangle$ was subtracted. In order to mimic observations, the resulting combined maps are smoothed with a Gaussian beam with a FWHM of $\sqrt{8\ln(2)}\,\sigma_b = 1$ arcmin.

In the case of multifrequency SZ observations the SZ signature can be easily distinguished from the CMB signal. Therefore, for these cases the CMB background is ignored and not included in the simulated cluster SZ images. Nevertheless, finite instrumental resolution was taken care of and the SZ maps were convolved with a Gaussian kernel of $\sqrt{8\ln(2)}\,\sigma_b = 1$ arcmin (FWHM). This approach is optimistic considering instrumental noise and point sources, which distort the SZ frequency dependence and provide additional flux at the SZ decrement frequencies. While the second effect primarily diminishes the SZ detectability, it too generates noise similar to instrumental noise as a result of the Poisson fluctuation of the number of sources within an aperture. A detailed discussion can be found in Section 5.8.

The beam width was assumed to be 1 arcmin (FWHM), which is a reasonable choice considering the design values of currently planned dedicated SZ telesopes. These experiments are able to marginally resolve clusters out to redshifts of $z = 0.7$: at these distances, the beam size (in terms of standard deviation) becomes comparable to the core sizes of the least massive clusters considered here. At the largest redshifts of $z \simeq 1.1$ examined in this paper, the beam is approximately twice as large as the cluster core.

5 ANALYSIS

In this section, the analysis is explained step by step. After introducing the wavelet families (Section 5.1), the wavelet spectrum and the parameters deduced from it are described (Sections 5.2 and 5.3). The correlations of the wavelet spectral parameters with physical quantities are discussed (Section 5.4). The measurement principle and the breaking of degeneracy is illustrated in Section 5.5. Next, the intercorrelation of the wavelet parameters and the shape of the parameter space are explored by principal component analysis (Section 5.6). Then, gauge functions for modelling the redshift dependence of the parameters are proposed (Section 5.7). Several issues for observers are discussed in Section 5.8, for instance the influence of instrumental noise (Section 5.8.1), the influence of primary CMB fluctuations on the wavelet spectrum and their suppression (Section 5.8.2), and the impact of submillimetre point sources on the wavelet estimation technique (Section 5.8.3). Finally, the redshifts of the clusters are estimated by maximum likelihood techniques (Section 5.9).

5.1 Wavelet basis functions

In the analysis, a wide range of wavelets with different functional shapes was employed, although the symlet wavelet basis introduced by Daubechies & Bates (1993) yielded particularly good results. Owing to their symmetry and peaked nature, symlets are seemingly especially suited for analysing SZ morphologies, because they do not impose a strong smoothing on the image in determining the wavelet moments $X_q(\sigma)$. Other wavelet families that found application in our analysis were Daubechies' wavelets, coiflets and biorthogonal wavelets. Fig. 5 compares the functional shapes of the various wavelet families.

The analysis proceeds by measurement of the wavelet moments on smoothed comoving maps of the Compton-y parameter following the definition in Section 3. The scale σ of the resulting wavelet spectrum is then converted to angular units. Because our SZ maps are computed on a grid of 128^2 mesh points with an adaptively chosen side length for each cluster, our dynamical range of the wavelet spectra always comprises approximately two decades. However, this is not a fundamental limitation of this approach because the maps are featureless below the smoothing scale of 1 arcmin (FWHM).

5.2 Measurement of wavelet quantities

In order to derive the actual flux decrement or, equivalently, the decrement in antenna temperature, from the line-of-sight Compton-y amplitude, the pixel value needs to be multiplied by the solid angle it subtends. For the conversion, a standard ΛCDM cosmology was assumed, the parameters of which have already been given in

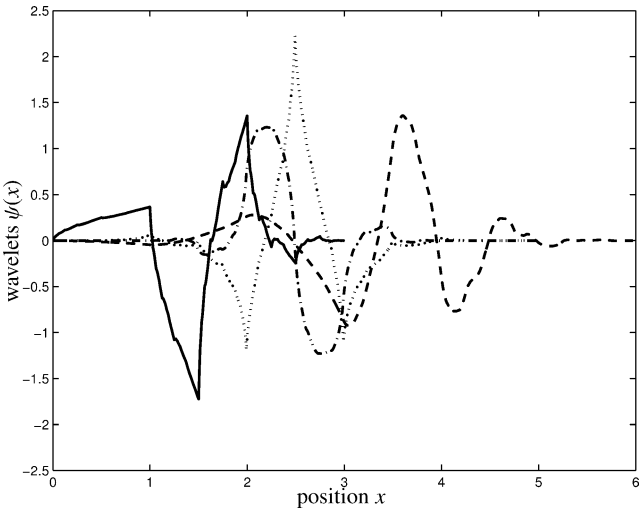

Figure 5. The wavelet basis functions $\psi(x)$ chosen for the analysis: symlet (*sym2*, solid), Daubechies' wavelet (*db4*, dashed), coiflet (*coif1*, dotted) and the biorthogonal wavelet (*bior1.3*, dot–dashed).

Section 4. Thus, the pixel amplitudes were modified according to

$$y(\boldsymbol{x}) \longrightarrow y(\phi) = y(\boldsymbol{x}) \cdot 4 \arctan^2 \left[\frac{g}{2w(z)} \right], \tag{32}$$

where $w(z)$ is the comoving distance in the model cosmology and g denotes the comoving size of a single pixel. It should be emphasized that the wavelet coefficients $\chi(\boldsymbol{\mu}, \sigma)$ are evaluated on a comoving grid, which is adapted to the cluster size before conversion of the wavelet scale σ to angular units. This, however, should not pose a problem for real observations, provided that the sampling scale is of the same order of magnitude as the angular scale of our finest pixels.

In order to obtain dimensionless quantities, the unit of the wavelet $\psi_\sigma(\boldsymbol{x})$ has been set to inverse steradians, such that the wavelet expansion coefficients $\chi(\boldsymbol{\mu}, \sigma)$ and the wavelet moments $X_q(\sigma)$ are dimensionless, irrespective of q. For numerical convenience, the pixel amplitudes in the combined SZ maps have been multiplied by 10^{12}, which scales the pixel amplitudes to be of order unity.

The summation in the definition of the wavelet moment $X_q(\sigma)$ in equation (4) discards the information about the position $\boldsymbol{\mu}$ at which the wavelet expansion coefficient $\chi(\boldsymbol{\mu}, \sigma)$ is evaluated. Consequently, the position of a cluster inside the observing frame does not influence the wavelet decomposition.

5.3 Wavelet spectrum of SZ cluster maps

Owing to the lack of any analytical generalization of equation (17) for $q \neq 2$, to deviations of the Compton-y map from a King profile and to the use of wavelets other than the simple Mexican hat, we decided to explore phenomenological functions for describing the wavelet spectrum. The simplicity of the shape of the wavelet spectrum shown in Fig. 6 implies that the model function,

$$\ln X_q(\sigma) \simeq a + s \ln(\sigma/\sigma_0) - \sigma/c, \tag{33}$$

is able to extract all apparently contained information. In other words, the spectrum is described by means of three quantities: the amplitude a, the slope s and a break at c. The parameter σ_0 has been included in equation (33) in order to obtain a formula that is dimensionally correct, although it does not yield any new information, and this specific degree of freedom is already described by the variable a.

The usage of equation (33) implicitly neglects information about asphericity and effectively determines an average of the cluster's extension along its major axes. The problem would be significantly complicated by including asymmetry and considering the vectorial nature of σ (see Zaroubi et al. 1998, 2001).

Because the cut-off parameter c is of great importance to our analysis, it needs to be derived reliably. Thus, the order of wavelet moments q was restricted to $q \geqslant 3$, because larger q-values facilitate the determination of c. From Fig. 6 it is obvious that an increase in q suppresses the value of $X_q(\sigma)$ at small scales σ such that the curve develops a maximum in the vicinity of c. In addition, by the choice of large values for q, the wavelet expansion coefficients $\chi(\mu, \sigma)$ dominated by CMB noise are suppressed relative to those obtained in the central part of the cluster, and consequently higher-order wavelet moments $X_q(\sigma)$ provide a cleaner measurement. The range of sensible q-values is restricted by the fact that for increasing q the moment $X_q(\sigma)$ is successively dominated by the largest wavelet expansion coefficient $\chi(\mu, \sigma)$ and no longer contains information of the structure to be analysed. In order to stabilize the fitting procedure we interpolate in between the wavelet moments $X_q(\sigma)$. This is justified because we expect a smooth variation of the wavelet spectrum, according to Section 3.2.1.

5.4 Correlations with physical quantities

The parameters derived from the fit to the spectrum of wavelet coefficients have a physical interpretation. As shown in Section 3.2.1, the wavelet spectrum breaks at the cluster scale. Therefore, a correlation is expected between the angular size of the cluster $\theta_{\rm vir}$ and the cut-off c, as found in Fig. 7. Larger values of the weighting exponents q shift the regression line to smaller values of c, which can be understood by the fact that larger values of q suppress small wavelet expansion coefficients arising at the outskirts of the cluster, which in turn leads to a break in the wavelet spectrum at smaller scales.

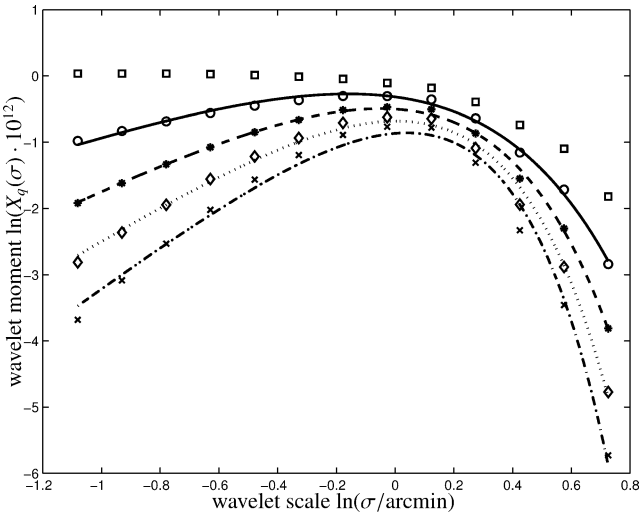

Figure 6. The spectrum of wavelet moments, together with the fitting formula (33) for increasing wavelet moment order q: $q = 2$ (squares), $q = 3$ (circles, solid), $q = 4$ (stars, dashed), $q = 5$ (diamonds, dotted) and $q = 6$ (crosses, dot–dashed) for a single cluster. The wavelet moments $X_q(\sigma)$ follow from wavelet expansion with the *sym2*-wavelet.

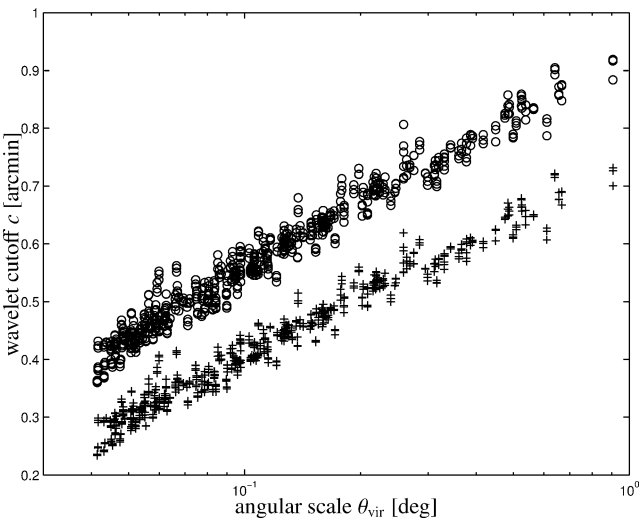

Figure 7. Wavelet-measured cluster size c versus angular extension $\theta_{\rm vir}$ for increasing wavelet moment order q: $q = 3$ (circles) and $q = 6$ (crosses), without including CMB fluctuations. The c-values were determined with the *sym2*-wavelet.

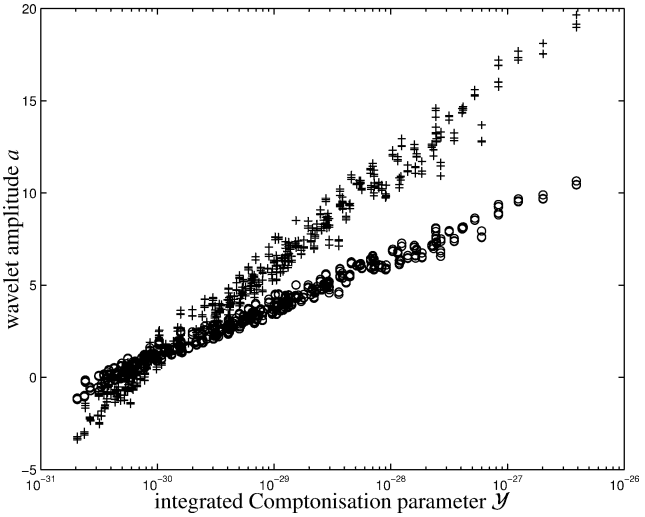

Figure 8. Wavelet amplitude a as a function of the integrated Comptonization parameter $\mathcal{Y}$ for various weighting exponents q: $q = 3$ (circles) and $q = 6$ (crosses), again without taking CMB fluctuations into account. The *sym2*-wavelet was chosen as the analysing wavelet.

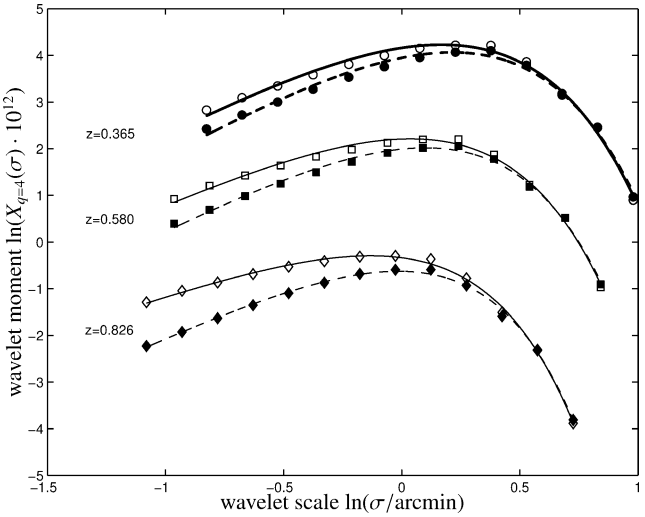

Figure 9. Wavelet spectra $X_4(\sigma)$ of three clusters at redshifts $z = 0.365$ (circles, thick lines), $z = 0.580$ (squares, medium lines) and $z = 0.826$ (diamonds, thin lines), where instrumental smoothing has been ignored (open symbols, solid lines) and properly taken account of (closed symbols, dashed lines). The spectra were derived with the *sym3*-wavelet as the analysing wavelet.

Similarly, the amplitude a determined by the fit is proportional to the integrated Compton-y flux,

$$\mathcal{Y} = \int \mathrm{d}^2\phi\; y(\phi) = \frac{kT_{\mathrm{vir}}}{m_{\mathrm{e}}c^2}\,\frac{\sigma_T}{d_{\mathrm{A}}(z)^2}\,\frac{1+f_{\mathrm{H}}}{2}\,f_{\mathrm{b}}\,\frac{M_{\mathrm{vir}}}{m_{\mathrm{p}}}, \tag{34}$$

as illustrated in Fig. 8. Here, f_{b} denotes the baryon fraction, f_{H} the hydrogen fraction, which determines the elemental composition and has been set to the primordial value of 0.76, and m_{p} is the proton mass. $d_{\mathrm{A}}\,(z)$ is the angular diameter distance in our cosmology.

The normalization a of the wavelet moments $X_q(\sigma)$ shows a steeper dependence on the integrated Comptonization parameter $\mathcal{Y}$ for larger choices of q, which is explained by the following argument. The amplitude $a(q)$ reflects the normalization of the wavelet moments $X_q(\sigma)$. The integral in equation (4) is dominated by the largest wavelet expansion coefficient $\chi(\boldsymbol{\mu}, \sigma)$, taken to the qth power. On the other hand, the wavelet expansion coefficients $\chi(\boldsymbol{\mu}, \sigma)$ are proportional to the integrated Comptonization parameter $\mathcal{Y}$, resulting in the observed relation $\ln\left[X_q(\sigma)\right] \propto a \propto q\,\ln(\mathcal{Y})$. As a summary, Fig. 9 shows the wavelet spectra for three comparable clusters situated at different redshifts, taking instrumental smoothing into account. The figure illustrates how the amplitude and the break of the spectrum decrease with increasing redshift.

The influence of instrumental smoothing on the wavelet parameters can be summarized as follows. In the case of suppressed noise, the amplitude a, being a measurement of $\mathcal{Y}$, should be still reliably measurable, in contrast to, for example, isophotal flux or related quantities, despite the fact that it is systematically smaller owing to the instrumental beam. The angular size, however, expressed by the cut-off c, increases with increasing smoothing, but can still serve as a measure for cluster size even in cases in which the size of the instrumental beam becomes comparable to the cluster core. In addition, this behaviour is supported by Fig. 10, in which a weak deviation from proportionality towards larger values of c is easily visible. Nevertheless, the value of c does not deteriorate significantly as a result of the instrumental smoothing.

Finally, the slope s is purely a measure of instrumental smoothing. Placing a given cluster at different redshifts would result in a blurred image of the more distant one. Keeping in mind that there is a close analogy between wavelet and Fourier transforms (as explained in Section 3.3), the wavelet moment $X_q(\sigma)$ as a function of σ can be interpreted as the variance of the wavelet-filtered field. The instrumental beam introduces an additional filtering to the Compton-y map (cf. Section 3.2.3) and would cause the Fourier spectrum to drop at smaller values of the wavevector k, because the instrumental beam constitutes effectively a low-pass filter that erases structures smaller than its extension. Comparing clusters at different redshifts, it is clear that the drop in power happens at smaller scales in the case of the more distant clusters. Thus the slope s, defined as $\mathrm{d}\ln X_q(\sigma)/\mathrm{d}\ln\sigma$ for $\sigma \ll r_{\mathrm{c}}$, is larger in the case of an unresolved cluster compared with a resolved cluster. This measure of the influence of finite instrumental smoothing varies only by a factor of 2 in slope over the redshift and mass ranges considered here, but nevertheless

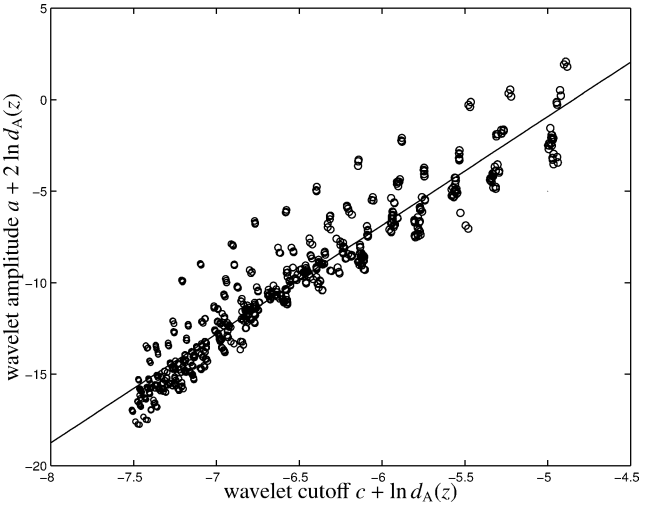

Figure 10. Distance-corrected wavelet amplitude $a_0 = a(z) + 2\ln(d_{\mathrm{A}}(z))$ as a function of the distance-corrected wavelet cut-off parameter $c_0 = c(z) + \ln(d_{\mathrm{A}}(z))$. The values have been determined in fits to the wavelet spectrum $X_3(\sigma)$, which was derived with the *sym2*-wavelet as the analysing wavelet.

serves as an indicator of cluster distance. It should be emphasized that the *s*-parameter does not try to extract information from scales that are inaccessible as a result of instrumental smoothing. Wavelet analysis of maps that are poor in features over a certain range of scales generically results in power laws for $X_q(\sigma)$ for these scales.

5.5 Measurement principle

Now, it is necessary to illustrate how a measurement of the total Comptonization $\mathcal{Y}$ and of the angular size $\theta_{\rm vir}$ suffices to derive a distance estimate. For that purpose, clusters are placed at unit distance and the distance dependences of the wavelet amplitude a and the cut-off c are removed by the following formulae, since a is a logarithmic measure of flux inside a solid angle element $\mathcal{Y}$ and c is a logarithmic measure of angular extension $\theta_{\rm vir}$:

$$a_0 = a(z) + 2\,\ln\left(d_A(z)\right), \tag{35}$$

$$c_0 = c(z) + \ln\left(d_A(z)\right). \tag{36}$$

From the application of simple scaling arguments, the ratio a_0/c_0 is expected to be equal to 5. From the wavelet amplitude a one obtains $a_0 \propto \ln(\mathcal{Y}\, d_{\rm A}(z)^2) \propto \ln(M_{\rm vir}\, T_{\rm vir})$. Furthermore, from the spherical collapse model it follows that $T_{\rm vir} \propto M_{\rm vir}^{2/3}$ (Navarro et al. 1995), which yields, together with $M_{\rm vir} \propto r_{\rm vir}^3$, the relationship $a_0 \propto \ln(r_{\rm vir}^5)$. Substituting $c_0 \propto \ln(r_{\rm vir})$ gives the final result $a_0/c_0 = 5$.

Fig. 10 nicely illustrates how the degeneracy is broken and how a simple measurement of flux and angular extension suffices to derive a distance estimate. A crude fit to the distance-corrected wavelet amplitude a_0 as a function of distance-corrected wavelet cut-off parameter c_0 yields a slope of approximately 5.8, which corresponds well to the slope of $\sim$5 expected from the theoretical consideration outlined above. If, hypothetically, the ratio a_0/c_0 were equal to 2, the measurements of flux and angular size would be completely degenerate and would not yield any distance information. This case corresponds to discs of equal surface brightness, for which measurements of flux and angular size are completely degenerate and do not yield any distance information at all. It should be noted that, by adopting the usual scaling relations, a systematic error in slope is introduced that can amount to $\simeq$20 per cent.

5.6 Principal component analysis

In order to investigate the shape of the parameter space spanned by the three morphological descriptors a, c and s derived in the fit to the spectrum of wavelet moments, a principal component analysis (PCA; see, for example, Deeming 1964) was performed. PCA determines a transformation to a new orthogonal coordinate system, such that the variance of the data along the first axis is maximized. In this way, the correlation properties, the effective dimensionality and the redundancy of the parameters can be quantified.

From the fact that the first principal component is able to account for almost the entire variance of the data set, as can be seen from Table 1, it can be concluded that the parameter space is tightly constrained and all three parameters are interrelated. This result holds irrespective of the choice of q, although the scatter increases with higher choices for q. Given the physical interpretations of the wavelet amplitude a and the cut-off c, it is obvious that the tight correlation can be traced back to the self-similarity of clusters and the cluster scaling relations linking $T_{\rm vir}$, $M_{\rm vir}$ and $r_{\rm vir}$ that follow from the spherical collapse model, together with the dependence of these parameters on the redshift. The scaling relations for SZ quantities derived by da Silva et al. (2004) support this view. Furthermore, PCA suggests that all three fundamental parameters depend on the redshift in a similar way, as will be shown in the next section.

Table 1. Results of the PCA. The variance explained by the first and second principal components as a function of wavelet order q. The *sym2*-wavelet was used as the analysing wavelet, and no CMB fluctuations were included in the derivation.

	$q=3$	$q=4$	$q=5$	$q=6$
1st principal component (per cent)	95.6	94.2	92.8	91.5
2nd principal component (per cent)	2.7	4.2	5.5	6.7

5.7 Redshift dependence of the wavelet parameters

The parameters a and c are expected to decrease with increasing redshift z, the reason for which is quite apparent: the angular diameter $\theta_{\rm vir}$ and the integrated Comptonization $\mathcal{Y}$ decrease because of the increasing angular diameter distance $d_{\rm A}(z)$ that enters $\theta_{\rm vir}$ linearly and $\mathcal{Y}$ quadratically. Furthermore, clusters accrete matter during their formation history and thus are on average more massive at later times, i.e. at smaller redshifts z (see, for example, Wechsler et al. 2002; van den Bosch 2002; Zhao et al. 2003). From the physical point of view, the dependence of a and c on redshift z is far from trivial, and, therefore, their functional behaviour is described by an empirical approach. Among others, the exponential function provides a good fit to the data, as illustrated in Figs 11 and 12:

$$x(z) = x_1 \exp\left(-\frac{z}{x_2}\right) + x_3, \text{ where } x \in \{a, c, s\}. \tag{37}$$

The optimized parameters x_i, $i \in \{1, 2, 3\}$, for $x \in \{a, c, s\}$ in the gauge function equation (37) are given in Table 2 for the case $q = 3$. It should be emphasized that the parameters stated are only valid for image analysis with the *sym2*-wavelet, where the maps have been smoothed with a Gaussian kernel with 1-arcmin (FWHM), and the considered cluster sample, which is defined by the

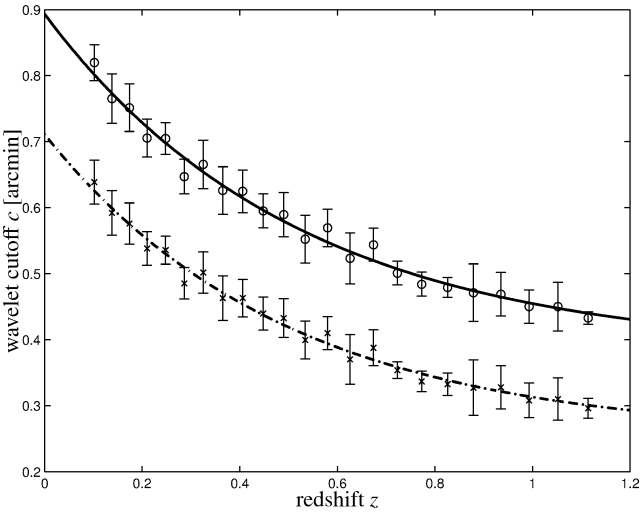

Figure 11. Dependence of the wavelet cut-off parameter c on redshift z without considering CMB fluctuations for $q = 3$ (circles, solid) and $q = 6$ (crosses, dot–dashed line). The analysing wavelet was the *sym2*-wavelet.

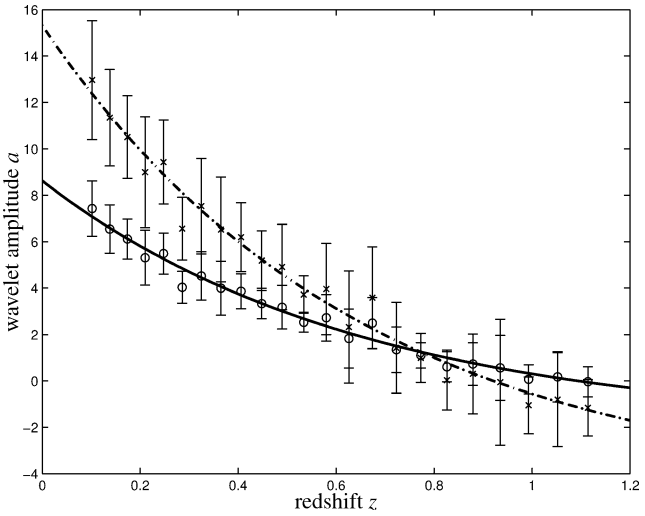

Figure 12. Dependence of the wavelet amplitude parameter a on redshift z without including CMB fluctuations for $q = 3$ (circles, solid) and $q = 6$ (crosses, dot–dashed line). The quantities were determined with the *sym2*-wavelet.

Table 2. Fitting values for the gauge functions defined in equation (37) for the cluster sample at hand and the *sym2*-wavelet basis. The order of the wavelet moment $X_q(\sigma)$ has been set to $q = 3$. The values have been derived without taking CMB fluctuations into account.

Parameter	Variable	$i = 1$	$i = 2$	$i = 3$
Amplitude	a	10.5837	0.6475	−1.9570
Cut-off (arcmin)	c	0.5124	0.5165	0.3809
Slope	s	1.3423	0.4144	1.3803

selection criteria laid down in Section 4.3 and the minimal mass of $5 \times 10^{13}\,\mathrm{M}_\odot\,h^{-1}$.

5.8 Noise contributions and their suppression

5.8.1 Influence of instrumental noise

The extent to which the wavelet spectra are affected by instrumental noise is a very important issue. Even though experiments such as the ACT aim at achieving noise levels as low as $\sigma_\mathrm{T} \simeq 2$–$5\,\mu\mathrm{K}$ per 3 arcmin^2-pixel (depending on the channel, Kosowsky 2004), instrumental noise nevertheless impacts on the shape of the wavelet spectra. Fig. 13 shows the distorted wavelet spectra for two wavelet families on SZ maps where uncorrelated pixel noise at a level equivalent to (a pessimistic value of) $\sigma_\mathrm{T} = 10\,\mu\mathrm{K}$ per square arcminute has been added.

Instrumental noise can be characterized by an approximately power-law component in the spectrum of wavelet coefficients $X_q(\sigma)$. The influence of the noise on the wavelet spectrum is small and can be suppressed either by choosing large q or by employing a smoothly varying wavelet, for instance a member of the symlet family instead of a peaked wavelet, such as the coiflet. Furthermore, the instrumental noise does not cause a significant deviation of the model parameters a, c and s once the detection of the cluster is sufficiently reliable, i.e. exceeding a value of 10σ, which is the case even for the least massive clusters in our sample out to redshifts of $z = 0.8$. At even higher redshifts, wavelet analysis will be seriously impeded by instrumental noise.

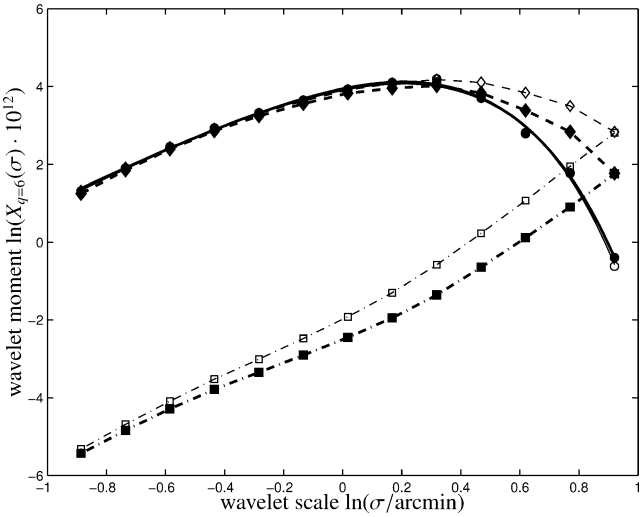

Figure 13. Changes to the wavelet spectrum of a single cluster (situated at $z = 0.49$) caused by instrumental noise: unperturbed wavelet spectrum of the SZ cluster (circles, solid line), of pure instrumental noise (squares, dot–dashed line) and of the combined map (diamonds, dashed line). Data points were derived from simulated data and the joining line in the case of the unperturbed wavelet spectrum is the result of the fitting functions described by equation (33). The order of the wavelet moment is $q = 6$. As analysing wavelets, the *sym3*-wavelet (thick lines, closed symbols) and the *coif1*-wavelet (thin lines, open symbols) are compared.

5.8.2 Influence of CMB fluctuations

Clusters at high redshift z are characterized by their small angular scale on which the underlying CMB is represented by a smooth gradient as a result of Silk damping (Silk 1968). In this case the wavelet analysis produces the same results irrespective of the CMB noise owing to the distinct morphological feature of the cluster on top of the smooth CMB gradient. Once clusters at lower redshifts reach angular sizes comparable with characteristic scales of CMB fluctuations, the wavelet analysis has to be made more sophisticated. This complication in the wavelet analysis arises because wavelets are primarily suited for determining morphological features rather than singling out high-amplitude characteristics. Because the angular scale of the clusters ranges between 10 and 1 arcmin, which corresponds to multipole orders of $\ell \simeq 10^3 \ldots 10^4$, it suffices to consider the Silk-damping tail of the angular power spectrum of the CMB. In the wavelet spectrum $X_q(\sigma)$ this translates into an additional approximately power-law component $X_q^\mathrm{CMB}(\sigma)$, as can be seen from Fig. 14:

$$\ln X_q^\mathrm{CMB}(\sigma) \simeq a_\mathrm{CMB} + s_\mathrm{CMB} \ln\sigma\,. \tag{38}$$

This is a result of the discrete sampling of the wavelet moments as well as of the inherent statistics of the wavelet spectra of order q, which can be interpreted as suitably weighted q-point correlation functions in Fourier analysis (cf. Section 3.3).

Fig. 15 shows the probability distribution function $p(s_\mathrm{CMB})\mathrm{d}s_\mathrm{CMB}$ of the slopes s_CMB following from linear fits to the wavelet moments $X_q(\sigma)$ for the range of qs considered here. Again, the *sym2*-wavelet was chosen as the analysing wavelet. The slopes s_CMB are not well confined, keeping the vast range of angular scales in mind, which in turn will make it difficult to subtract the CMB contribution to the wavelet spectrum of the combined map.

In order to untangle the contributions from the CMB noise from those of the cluster, one can pursue a variety of approaches. For

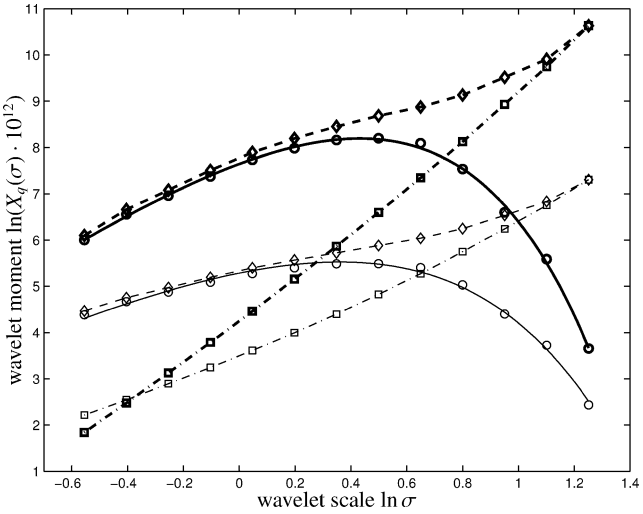

Figure 14. Changes to the wavelet spectrum of a single cluster caused by the fluctuating CMB: unperturbed wavelet spectrum of the SZ cluster (circles, solid lines), of the pure CMB (squares, dot–dashed lines) and of the combined map (diamonds, dashed lines). Data points were derived from simulated data and the joining line in the case of the unperturbed wavelet spectrum is the result of the fitting functions described by equation (33). The order of the wavelet moment is $q = 6$ (thick) and $q = 4$ (thin). Again, the analysing wavelet was the *sym2*-wavelet.

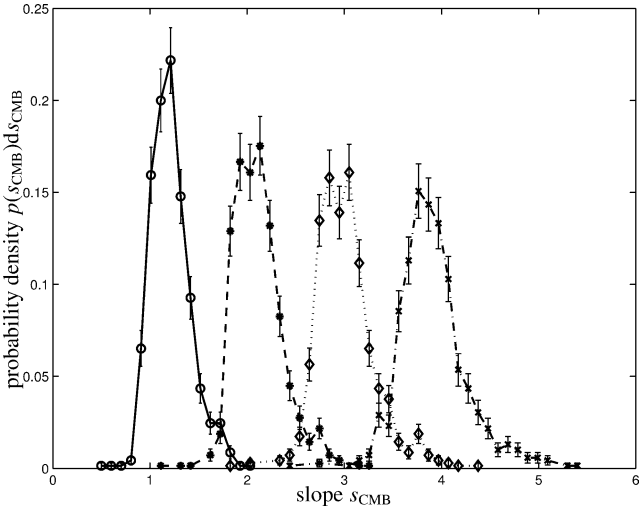

Figure 15. Distributions of the power-law slopes $s_{\rm CMB}$ of CMB wavelet spectra as a function of wavelet moment order: $q = 3$ (circles, solid line), $q = 4$ (stars, dashed line), $q = 5$ (diamonds, dotted line), $q = 6$ (crosses, dot–dashed line). The analysing wavelet is the *sym2*-wavelet.

example, CMB fluctuations underneath the cluster can be reconstructed with spline polynomials and successively subtracted. Here, we have masked the cluster and fitted 5th-order polynomials to the remaining data points. Because the y-maps and the realizations of the CMB are to leading order combined linearly, and because the CMB is a smoothly varying field, it is possible to reconstruct the CMB fluctuations from the environment of the cluster and interpolate to the cluster centre. The reconstructed CMB field can be subtracted from the initial image, and, by applying wavelet decomposition to the cleaned field, it is possible to obtain a wavelet spectrum, from which the parameters a, c and s can be reliably derived.

An important question common to the suppression of the CMB and instrumental noise is the choice of a cluster mask region, either for reconstructing the ambient CMB fluctuations with polynomials or for reducing the contribution of pixel noise (which is proportional to the map area) to the wavelet spectrum. As soon as the cluster is detected at sufficient significance levels, it should be possible to choose the cluster mask region according to a preliminary determination of the cluster size. Choosing too large a mask region results in higher amplitudes of $X_q(\sigma)$ at large angular scales σ, but the parameters of the model function a and c are relatively insensitive to $X_q(\sigma)$ at large σ. Furthermore, it introduces a systematic trend in measurements of a and c, which could be taken account of by altering the functions that model the redshift dependence of those parameters.

5.8.3 Influence of point sources

Point sources such as infrared galaxies and microwave-emitting active galactic nuclei (AGNs) are yet another impediment to SZ observations. They influence SZ observations in two ways. First, the integrated flux of microwave sources inside the instrument's beam distorts the SZ flux modulation and diminishes the signal at SZ decrement frequencies. Secondly, the Poisson fluctuation in the number of sources inside the beam leads to an additional noise component. While the first effect concerns the detectability of SZ clusters, the second effect influences the wavelet analysis in a way similar to instrumental noise.

The integrated emission from unresolved infrared galaxies makes up the cosmic infrared background (CIB) (Puget et al. 1996; Lagache & Puget 2000), the fluctuations of which become important at frequencies above $\nu \simeq 100$ GHz (Aghanim, Hansen & Lagache 2004). Lagache (2003) and White & Majumdar (2004) have estimated the number counts of unresolved infrared galaxies at SZ frequencies. In the easiest case, the sources are uncorrelated and the fluctuations obey Poissonian statistics, but the inclusion of correlations is expected to boost the fluctuations by a factor of $\sim$1.7 (Song et al. 2003). According to Aghanim et al. (2004), the resulting fluctuations vary between a few 10^2 Jy sr^{-1} and 10^5 Jy sr^{-1}. A proper modelling would involve a biasing scheme for populating haloes, knowledge of the star formation history, and template spectra in order to determine the K-corrections.

In AGNs, the situation is similarly complex: the spectra show a variety of functional behaviours, with spectral indices α generally ranging from -1 to -0.5, but sources with inverted spectra $\alpha > 0$ are commonplace. This variety makes it difficult to extrapolate fluxes to the observing frequencies of CMB experiments. Two studies (Toffolatti et al. 1998; Sokasian, Gawiser & Smoot 2001) have estimated the fluctuations generated by radio-emitting AGNs at SZ frequencies and found them to amount to 10^3–10^4 Jy sr^{-1}. However, AGNs are known to reside in high-density environments and the proper modelling would involve a biasing scheme in order to assign AGNs to the dark matter haloes. Apart from that, one would have to assume spectral properties from a wide range of spectral indices and AGN activity duty cycles.

Given the poor experimental constraints, no attempt is made to model the influence of point sources on wavelet spectra. The additional noise component arising from the fluctuating number of point sources can be expected to influence wavelet spectra in a way

similar to instrumental noise, and therefore all proposed methods of suppression are applicable to this case as well.

5.9 Redshift estimation

In order to assess the accuracy of the redshift measurement, a maximum likelihood estimation is performed. The likelihood function is defined as

$$\mathcal{L}(z) = \frac{1}{(2\,\pi)^{3/2}\,\sigma_a\,\sigma_c\,\sigma_s}\,\exp\left(-\sum_{x\in\{a,c,s\}}\frac{1}{N}\sum_{i=1}^{N}\frac{(x_i - x(z))^2}{2\sigma_x^2}\right), \quad (39)$$

and was evaluated for each bin separately; in other words, the index i enumerates clusters within the redshift bin under consideration. $N = 30$ denotes the number of clusters within a single redshift bin. From the position of the maximum in $\mathcal{L}(z)$, the most probable redshift estimate z was derived and the accuracy of the estimate followed from the 1σ confidence intervals; that is, the accuracy is determined by the range in redshift z enclosing 68 per cent of the estimates. The function was found to be symmetric about the maximum value and hence the mean width is stated as the estimation accuracy. Fig. 16 shows the estimated redshift versus the real redshift for the cluster sample derived by using all three parameters a, c and s. In comparison, the error bars become larger by a factor of $\simeq$1.5 when including the fluctuating CMB, as illustrated by Fig. 17. The measurement is unbiased and the error relative to $1 + z$ rises slightly with increasing redshift z.

The results for the various analysing wavelets as a function of wavelet moment order q are summarized in Tables 3 and 4. Clearly,

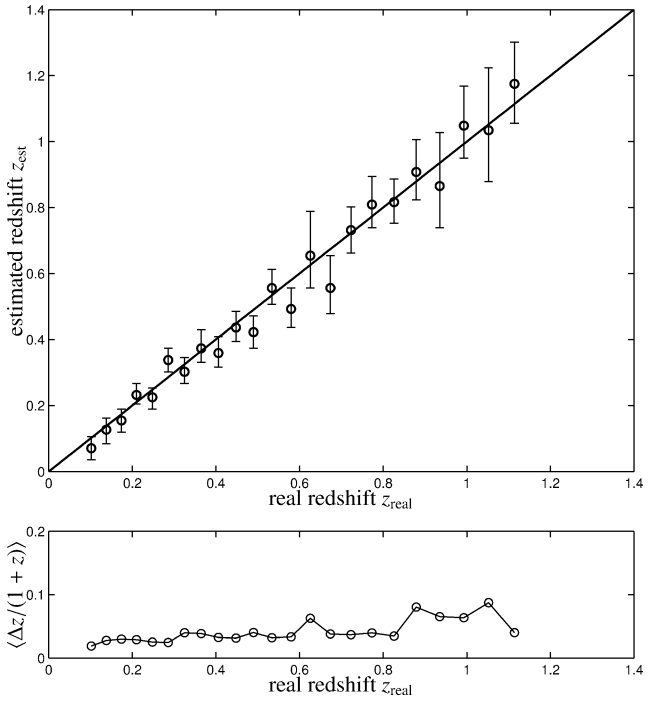

Figure 16. Redshift determination and error estimation from all three parameters a, c and s that followed from wavelet analysis with the *sym2*-wavelet. The upper panel shows the estimated redshift $z_{\rm est}$ and its error Δz, and the lower panel shows the relative accuracy $\Delta z/(1 + z)$, both as a function of redshift $z_{\rm real}$. Here, CMB fluctuations were not taken into account. The value of the wavelet moments was set to be $q = 3$.

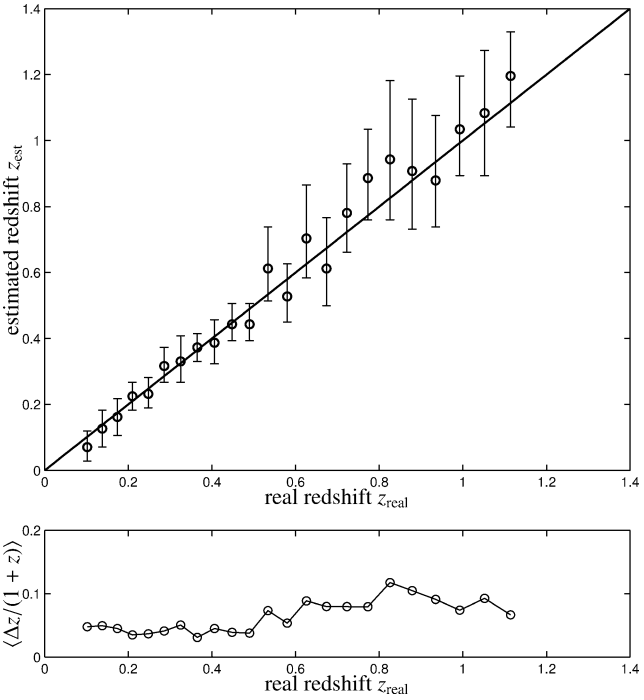

Figure 17. Redshift determination and error estimation from all three parameters a, c and s resulting from wavelet decomposition of the combined maps (i.e. with CMB) using the *sym2*-wavelet. In the upper panel, the estimated redshift $z_{\rm est}$ and its error Δz are shown as a function of real redshift $z_{\rm real}$. In comparison, the relative accuracy $\Delta z/(1 + z)$ as a function of $z_{\rm real}$ is shown in the lower panel. Again, the order of the wavelet moments was taken to be $q = 3$.

Table 3. Averaged accuracy (per cent) of the redshift determination relative to $1 + z$ based on three parameters derived from the wavelet spectrum of order q without the noise contribution from the fluctuating CMB.

Wavelet family	Wavelet	$q = 3$	$q = 4$	$q = 5$	$q = 6$
symlet	*sym2*	4.1	4.4	4.7	4.8
symlet	*sym3*	4.3	4.8	5.1	5.2
Daubechies'	*db4*	5.2	5.3	5.4	5.4
Daubechies'	*db5*	5.5	5.0	4.9	4.8
coiflet	*coif1*	4.2	4.4	4.8	5.0
biorthogonal	*bior1.3*	5.5	5.4	5.4	5.4

Table 4. Averaged accuracy (per cent) of the redshift determination relative to $1 + z$ based on three parameters derived from the wavelet spectrum of order q with the noise contribution caused by fluctuations in the CMB.

Wavelet family	Wavelet	$q = 3$	$q = 4$	$q = 5$	$q = 6$
symlet	*sym2*	6.2	6.3	6.2	6.3
symlet	*sym3*	6.7	6.5	6.4	7.2
Daubechies'	*db4*	6.9	6.8	6.9	6.9
Daubechies'	*db5*	7.6	7.4	7.3	7.2
coiflet	*coif1*	6.1	5.9	6.0	6.8
biorthogonal	*bior1.3*	7.5	7.4	7.2	7.3

the method starts to fail at redshifts $\gtrsim$1, when the angular diameter distance $d_{\rm A}(z)$ develops a plateau and does not cause clusters to appear smaller. The average attainable accuracy is stated relative to $1 + z$ in order to facilitate comparison with photometric redshifts.

The accuracy degrades slightly with increasing q, which is the result of the suppression of small wavelet expansion coefficients, especially at small scales, and the resulting inaccuracy of the fitting formula (equation 33) used to extract the spectral parameters a, c and s from the wavelet spectrum.

Inclusion of the CMB in order to test the applicability of determining morphological redshifts in the case of single-frequency interferometers results in a deterioration of the redshift estimation accuracy by a factor of close to 1.5. This is caused by imperfections of the CMB removal by 5th-order spline polynomials.

It should be kept in mind that the given accuracy estimates depend on the proprties of the selected cluster sample. The insufficient sampling of the high-mass end of the Press–Schechter function can, in particular, be expected to play a significant role, and leads to a systematic underestimation of the redshift accuracy.

6 SYSTEMATICS

SZ clusters would be self-similar and would perfectly follow scaling relations provided several requirements were fulfilled, namely (i) virial equilibrium ($T \propto M^{2/3}$); (ii) structural identity, expressed in equal form factors; (iii) a universal baryon fraction; and (iv) the absence of non-gravitative heating and cooling processes. Each of these assumptions can be challenged and leads to deviations from the self-similar scaling relationships. While the first two points are included in the numerical simulation and are limited by the selection criteria, they increase the scatter in the relationships between virial quantities, or, equally, between the wavelet parameters a, c and s. Systematic trends caused by tilted scaling relationships (see Section 6.1) and the formation of cool cores (formerly referred to as cooling flows) (Section 6.2) as well as the necessity of preselecting clusters (Section 6.3) need to be addressed separately.

6.1 Influence of tilted scaling relations

Analyses of X-ray observations carried out by Arnaud & Evrard (1999) and Mohr, Mathiesen & Evrard (1999) suggest a weak trend of the cluster baryon fraction with cluster mass M and a deviation from the universal value $f_\mathrm{b} = \Omega_\mathrm{b}/\Omega_\mathrm{m}$. This is the result of feedback processes such as galactic winds that more effectively deplete the ICM of baryons in low-temperature clusters compared with that in high-temperature clusters.

The dependence, in particular, of the wavelet parameter a, which is a logarithmic measure of the SZ flux $\mathcal{Y}$, would be increased in more massive clusters and would thus increase the scatter in a of a cluster sample at a given redshift. The quoted analyses of X-ray data find the baryon fraction to show a relative variation amounting to $\simeq$10 per cent at fixed temperature, i.e. at a fixed depth of the potential well for a sample of local clusters. Apart from the systematic component, which can in principle be removed, once high-quality X-ray data improves our understanding of this phenomenon and allows proper modelling, the stochastic contribution can only be constrained to be at most of equal relative influence to $\Delta\mathcal{Y}/\mathcal{Y}$ as the scatter in morphology.

The baryon fraction is estimated from X-ray observations that sample the gas at the cluster core, whereas the SZ effect will be sensitive to the gas at much larger scales. Therefore, since the observed trend is probably the result of the complicated hydrodynamic and feedback processes at the cluster centre, the trend is expected to be much weaker on the scales probed by the SZ effect.

6.2 Cool cores of clusters

In order to estimate the accuracy of the method outlined above, we have so far used only non-radiative hydrodynamical simulations that lack cooling processes. Thus we need to address the influence of the cool cores of clusters on our proposed method. After an analytical investigation following Section 3.2.1 we compare clusters with and without cool cores and show how the morphological changes in cool-core clusters affect the wavelet spectra.

6.2.1 Analytical wavelet transform of cool-core clusters

Instead of a single King profile we assume that the SZ emission of a cool-core cluster can be described by a double King profile for reasons of analytical feasibility:

$$y(\boldsymbol{x}) = y(r) = \sum_{i=1}^{2} y_i \left[1 + \left(\frac{r}{r_i}\right)^2\right]^{-1}, \tag{40}$$

where the second term describes the additional enhancement owing to the cool core. Deprojection of this two-dimensional profile by means of Pfrommer & Enßlin (2004) yields

$$p_\mathrm{e}(R) = n_\mathrm{e}(R)\, k_\mathrm{B} T_\mathrm{e}(R) = \frac{m_\mathrm{e} c^2}{\sigma_\mathrm{T}} \sum_{i=1}^{2} \frac{y_i}{\pi r_i} \frac{\mathcal{B}\left(\frac{1}{2}, \frac{3}{2}\right)}{\left(1 + R^2/r_i^2\right)^{3/2}}, \tag{41}$$

where R denotes the three-dimensional radius and $\mathcal{B}(a, b)$ denotes the β-function (Abramowitz & Stegun 1965). Thus we obtain for the ratio of the central values of the Comptonization parameters y_i

$$\frac{y_2}{y_1} = \frac{p_2\, r_2}{p_1\, r_1} \sim \frac{1}{2}, \tag{42}$$

where we have inserted typical values for cool-core clusters, $p_2/p_1 \sim 3$ and $r_2/r_1 \sim 1/6$. The second-order wavelet moment of cool-core clusters can be obtained by analogy with the non-cool-core case:

$$X_2^\mathrm{CF}(\sigma) = 2\pi \int \mathrm{d}k\, k^5 \exp(-k^2\sigma^2) \left| y_1 r_1^2 K_0(k r_1) + y_2 r_2^2 K_0(k r_2) \right|^2. \tag{43}$$

This second-order wavelet moment shows an increasing amplitude and a decreasing cut-off parameter compared with the one without a cool core.

6.2.2 Numerical analysis

In order to scrutinize these findings we apply our method to non-radiative simulations of clusters to which we add an enhanced emission to mimic the SZ emission of the cool core. In Fig. 18, the resulting spectra of wavelet moments are shown together with the fitting formula (equation 33) for increasing wavelet moment order q.

It can clearly be seen in Fig. 18 that the enhanced emission arising from the cool core yields a slightly higher amplitude of the wavelet spectrum on small scales. Extracting information from the wavelet spectrum by means of equation (33) reveals slightly higher values for the amplitude a and smaller values for the cut-off c on the per cent level. However, this influence is minimized when considering finite instrumental resolution, particularly for high-redshift clusters. In any case, if a prominent cool core is sufficiently well resolved it could be masked and replaced by an interpolation in between the mask boundaries.

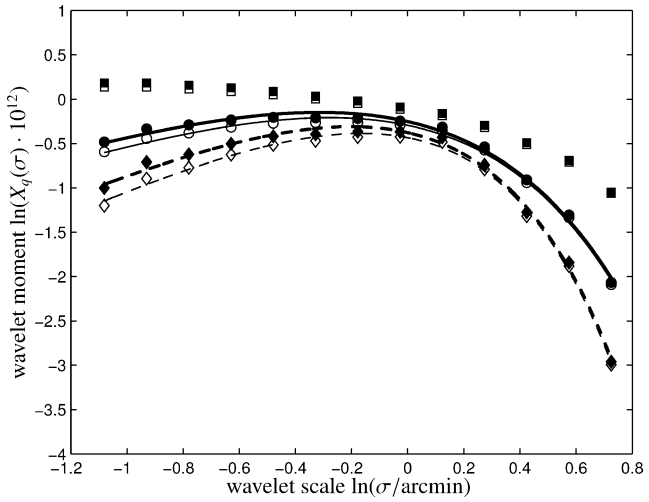

Figure 18. The influence of cool cores on the spectrum of wavelet moments, together with the fitting formula (33) for increasing wavelet moment order q: $q = 2$ (squares), $q = 3$ (circles, solid lines), and $q = 4$ (diamonds, dashed lines) for a single cluster without instrumental smoothing. Open symbols are values derived from the simulated non-cool-core cluster, whereas filled symbols denote the corresponding cool-core cluster.

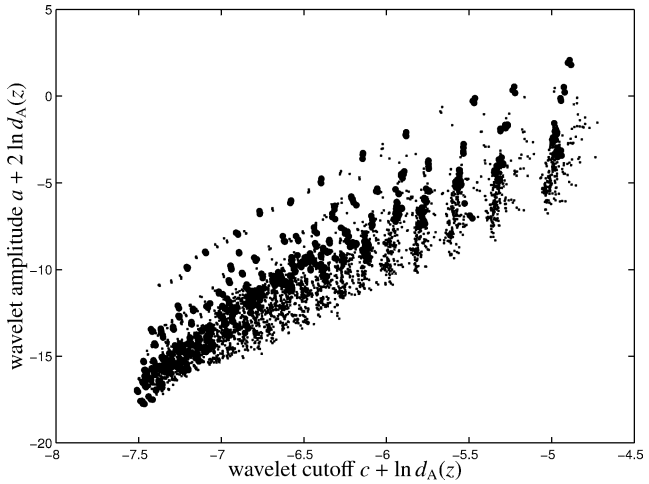

Figure 19. Distance-corrected wavelet amplitude $a_0 = a(z) + 2\ln(d_A(z))$ as a function of distance-corrected wavelet cut-off $c_0 = c(z) + \ln(d_A(z))$ for the selected clusters (circles) and all clusters (crosses) extracted from the simulation outputs. The wavelet moments $X_q(\sigma)$ were considered for $q = 4$, and the *sym3*-wavelet was employed as the analysing wavelet.

6.3 Wavelet analysis of unselected clusters

It is an important issue to quantify the deterioration of the wavelet method when applied to clusters of arbitrary morphology. In merging systems, for instance, one observes a doubly peaked wavelet spectrum, in which the peak at large σ reflects the angular size of the merger system itself, whereas the second peak at smaller σ corresponds to the scale of the merging objects. In these systems, the model function equation (33) does not yield a good fit to the spectrum of wavelet coefficients $X_q(\sigma)$ and hence fails to extract sensible values for the parameters a, c and s. Similarly, pronounced substructure causes deviations from the wavelet spectrum and yields additional power on scales smaller than the cluster scale. In these cases, the model function (cf. equation 33) does not necessarily provide a fit to the wavelet spectrum $X_q(\sigma)$ and it cannot be expected that the wavelet quantities a and c reflect cluster properties such as $\mathcal{Y}$.

In Fig. 19, the distance-corrected wavelet amplitude $a_0 = a(z) + 2\ln(d_A(z))$ is given as a function of the distance-corrected wavelet cut-off $c_0 = c(z) + \ln(d_A(z))$, for all clusters resulting from our simulation (in total 3957 maps) and, for comparison, for the selected subsample. The wavelet parameters were derived from a fit to the spectrum $X_q(\sigma)$ of order $q = 4$ with the sym3-wavelet as the analysing wavelet. While in Fig. 10 the data points follow a narrow track along $a \propto c^5$, this behaviour is not observed in Fig. 19. Especially for clusters at small wavelet cut-offs c, the scatter in wavelet amplitude a is doubled and data points fall below the region covered by the selected subsample. This might be hinting that clusters exhibit substructure, because in these cases the sizes are systematically underestimated by the fit to the wavelet spectrum $X_q(\sigma)$. Furthermore, a strong scatter in cut-off c is introduced. Given these significant deteriorations that can only be partially compensated by changes in the redshift model equation (37), the redshift estimation accuracy is significantly affected.

In comparison with the work of Diego et al. (2003), the distance estimation accuracy is almost doubled, which is partly the result of the selection of clusters. Only in systems with small deviations from spherical symmetry can the morphological parameters be reliably derived and used to indicate the cluster distance.

7 REDSHIFT ESTIMATION IN A NUTSHELL

This section will provide a short summary of how to apply our method to an SZ survey for estimating redshifts, providing a temperature map of a patch on the sky with resolved images of clusters.

(i) Once a cluster candidate has been localized at a particular position of the map, this cluster and its ambient field have to be cut out. If the number of grid points amounts to below 64^2 sampling points, the mesh should be refined by interpolation in order to reach a dynamical range of approximately two decades. This is important in order to provide a sufficiently broad range of scales to be probed by the wavelet decomposition.

(ii) The wavelet spectrum of the map is obtained by wavelet transforming the map, preferably using the symlet basis functions (see Section 3.1). The morphological information contained within the wavelet spectrum can be extracted by means of the model function of equation (33). In the case of single-frequency observations, the ambient CMB field cannot be separated from the SZ signal of a cluster. The method described in Section 5.8.2 might be applied in order to reconstruct the wavelet spectrum of the pure SZ cluster signal.

(iii) The redshift dependence of the wavelet parameters (amplitude a, cut-off c, and slope s) follows the functional form of equation (37). However, the single model parameters depend on the definitions of the particular wavelets and the details of the survey, including the various sources of noise and the cluster detection criteria. The most promising way of determining the parameters of the gauge functions laid down in equation (37) would be to derive them from a training set of clusters with known (photometric) redshifts. The final redshift estimate of the cluster is most conveniently determined by means of maximum likelihood analysis, as described by equation (39).

8 SUMMARY

In this paper, a method of estimating the redshift of a cluster based on the wavelet decomposition of its resolved SZ morphology is

presented. From a fit to the spectrum of wavelet moments three spectral parameters are derived, which in turn are non-degenerate and indicative of cluster distance. These parameters are utilized, through a maximum likelihood technique, to estimate the cluster's redshift. In the maximum likelihood technique, empirical gauge functions describing the wavelet parameter's z-dependence are used.

First, the method was tested on a simple analytical case. The spectrum of Mexican-hat wavelet moments can be derived analytically for a King profile, which is known to describe the Compton-y amplitude of clusters well. The spectrum of wavelet coefficients, as a function of wavelet scale σ, exhibits a break at the cluster scale r_c and may thus serve as a measure of the cluster's size. In addition, the asymptotic behaviour of the wavelet spectrum in the limits of $\sigma \gg r_c$ and $\sigma \ll r_c$ can be understood. The derivation of wavelet moments of order $q = 2$ is analogous to considering the Fourier power spectrum of the Compton-y map, filtered with Fourier transformed wavelet. The shape of the spectrum of wavelet moments of order $q = 2$ from the analytic calculation is consistent with one obtained by applying wavelet decomposition to simulated SZ cluster maps.

The method was then applied to set of numerically simulated SZ clusters with 1-arcmin (FWHM) resolution – comparable to the resolution of future SZ experiments. The sample comprises 690 cluster maps distributed in 23 redshift bins, which is a large cluster sample compared to other simulations. The clusters are chosen such that they are not in a merging state and their SZ image is not too elongated, two criteria that favour clusters close to virialization. Moreover, in order to simulate single-frequency observations, the cluster maps were combined with realizations of the CMB which constitutes the main source of noise.

The method was tested for a range of wavelet functions (e.g. symlet, coiflet, Daubechies, biorthogonal). The average attainable accuracy in estimating redshifts is found to be almost independent of the specific functional form used, although the symlet basis yielded the best results. However, the method could benefit from improvements concerning the choice of the wavelet basis. For instance, one could try to construct an optimized wavelet specifically for β-profiles that yields maximized wavelet coefficients $\chi(\mu, \sigma)$.

As expected, there is only a weak change in accuracy with respect to the order q of the chosen wavelet moment $X_q(\sigma)$. This, however, is likely to change when applying the wavelet analysis to noisy images, because, for higher values of q, uncorrelated noise is suppressed relative to the cluster's signal, and concentrating on higher values for q should provide a more robust measurement of the set of structural parameters a, c and s. The increment of q itself is limited by numerics – this is the case when the wavelet moment $X_q(\sigma)$ is dominated by the largest wavelet expansion coefficient $\chi(\mu, \sigma)$, and no longer reflects the dependence on the wavelet scale σ. In this limit, the wavelet spectrum would exhibit a generic power-law behaviour: $X_q(\sigma) \propto \sigma^{\gamma(q)}$ for large q. The structural parameters a, c and s were found to depend on redshift z by a simple exponential (equation 37). The free parameters in this equation can be determined from a (relatively small) sample of SZ cluster images with known redshift.

The accuracy of determining cluster distances has been assessed by maximum likelihood estimation. The method yields accuracies of 4–5 per cent relative to $1 + z$, which is competitive with photometric redshifts, but reaches out to larger distances. At redshifts of $z \gtrsim 1$, the accuracy is expected to degrade because the angular diameter distance $d_A(z)$ starts to level off and thus sets the limit of applicability. For single-frequency data, the CMB fluctuations can be removed with a simple polynomial reconstruction approach; the accuracy in the redshift estimation is then decreased to 6–7 per cent.

In this work we have considered two major systematic effects that might degrade the accuracy of the method. The first is the varying baryon fraction with cluster mass, which has been studied only for local cluster samples. While the systematic trend could in principle be corrected for, the stochastic contribution will always add to the uncertainty of the distance determination. Another systematic effect is the influence of cool cores at the cluster's centre. In this case we have been able to show that the uncertainty added to the redshift estimate is very small, mainly because the volume occupied by the cool-core region is limited to the cluster's core.

Although the result in the distance estimation is stated in terms of redshift, it should be emphasized that a specific cosmology is assumed, an assumption that is needed for converting the observables, namely the wavelet parameters, to a distance estimate. The distances following from the analysis have been expressed as redshifts because of their elementary interpretation, but the implicit assumption of an underlying cosmology should be kept in mind when comparing with, for example, photometric redshifts. For that reason, the precision of the method presented is limited by the accuracy to which the cosmological parameters are known. Apart from being a distance indicator, the redshift also plays the role of an evolutionary parameter.

Comparing this work with the pioneering paper by Diego et al. (2003), our expectations concerning the accuracy of morphological redshifts are even more optimistic: without fitting β-profiles to the observational data, it is possible to describe the cluster's SZ morphology solely by relying on wavelet decomposition. Furthermore, we describe the spectrum of wavelet moments with a small set of structural parameters that have a lucid physical interpretation, provide a non-degenerate distance measurement and enable redshift determination owing to their monotonic decline with redshift. The most important difference is that the redshift dependence of the structural parameters is calibrated with the data set itself, without the need for prior and simplifying assumptions. In spite of the small number of observables considered here, the accuracy in the redshift estimation of this method is doubled in comparison with that of Diego et al. (2003), even for a single-frequency experiment.

ACKNOWLEDGMENTS

The authors would like to thank Volker Springel and Lars Hernquist, who kindly provided us with their numerical simulations, and Antonaldo Diaferio, Matthias Bartelmann and Simon D. M. White for clarifying discussions and many useful comments. We thank the referees for the many detailed suggestions that improved the paper.

REFERENCES

Abramowitz M., Stegun I. A., 1965, Handbook of Mathematical Functions. Dover, New York
Aghanim N., Hansen S. H., Lagache G., 2004, A&A, in press (astro-ph/0402571)
Arnaud M., Evrard A. E., 1999, MNRAS, 305, 631
Bartelmann M., 2001, A&A, 370, 754
Bennett C. L. et al. 2003, ApJS, 148, 1
Birkinshaw M., 1999, Phys. Rep., 310, 98
Carlstrom J. E., Holder G. P., Reese E. D., 2002, ARA&A, 40, 643
Cavaliere A., Fusco-Femiano R., 1978, A&A, 70, 677
da Silva A. C., Kay S. T., Liddle A. R., Thomas P. A., Pearce F. R., Barbosa D., 2001, ApJ, 561, L15
da Silva A. C., Kay S. T., Liddle A. R., Thomas P. A., 2004, MNRAS, 348, 140

Daubechies I., Bates B. J., 1993, J. Acoust. Soc. Am., 93, 1671
Deeming T. J., 1964, MNRAS, 127, 493
Diego J. M., Mohr J., Silk J., Bryan G., 2003, MNRAS, 341, 599
Eke V. R., Cole S., Frenk C. S., Henry, P. J., 1998, MNRAS, 298, 1145
Gradshteyn I. S., Ryzhik I. M., 1994, in Jeffrey A., ed., Table of Integrals, Series and Products, 5th edn. Academic Press, New York
Haiman Z., Mohr J. J., Holder G. P., 2001, ApJ, 553, 545
Halverson N. W. et al., 2002, ApJ, 568, 38
Henry J. P., 2000, ApJ, 534, 565
Hu W., 2000, Phys. Rev. D, 62, 43007
Kosowsky A., 2004, New Astron. Rev., 47, 939
Lagache G., 2003, A&A, 405, 813
Lagache G., Puget J. L., 2000, A&A, 355, 17
Mohr J. J., Mathiesen B., Evrard A. E., 1999, ApJ, 517, 627
Monaghan J. J., Lattanzio J. C., 1985, A&A, 149, 135
Muzy J. F., Bacry E., Arneodo A., 1993, Phys. Rev. E, 47, 875
Navarro J. F., Frenk C. S., White S. D. M., 1995, MNRAS, 275, 720
Pfrommer C., Enßlin T. A., 2004, A&A, 413, 17
Puget J.-L., Abergel A., Bernard J.-P., Boulanger F., Burton W. B., Desert F.-X., Hartmann D., 1996, A&A, 308, L5
Rephaeli Y., 1995, ARA&A, 33, 541
Seljak U., Zaldarriaga M., 1996, ApJ, 469, 437
Silk J., 1968, ApJ, 151, 459
Sokasian A., Gawiser E., Smoot G. F., 2001, ApJ, 562, 88
Song Y., Cooray A., Knox L., Zaldarriaga M., 2003, ApJ, 590, 664
Spergel D. N. et al. 2003, ApJS, 148, 175
Springel V., Hernquist L., 2002, MNRAS, 333, 649
Sunyaev R. A., Zel'dovich I. B., 1972, Comm. Astrophys. Space Phys., 4, 173
Sunyaev R. A., Zel'dovich I. B., 1980, ARA&A, 18, 537
Toffolatti L., Argueso Gomez F., de Zotti G., Mazzei P., Franceschini A., Danese L., Burigana C., 1998, MNRAS, 297, 117
van den Bosch F. C., 2002, MNRAS, 331, 98
Wechsler R. H., Bullock J. S., Primack J. R., Kravtsov A. V., Dekel A., 2002, ApJ, 568, 52
White M., Majumdar S., 2004, ApJ, 602, 565
White M., Hernquist L., Springel V., 2002, ApJ, 579, 16
Zaroubi S., Squires G., Hoffman Y., Silk J., 1998, ApJ, 500, L87
Zaroubi S., Squires G., de Gasperis G., Evrard A. E., Hoffman Y., Silk J., 2001, ApJ, 561, 600
Zhao D. H., Mo H. J., Jing Y. P., Börner G., 2003, MNRAS, 339, 12

This paper has been typeset from a TEX/LATEX file prepared by the author.